

# Rotating toroids in G10.62–0.38, G19.61–0.23, and G29.96–0.02<sup>\*</sup>

M. T. Beltrán<sup>1</sup>, R. Cesaroni<sup>1</sup>, R. Neri<sup>2</sup>, and C. Codella<sup>1</sup>

<sup>1</sup> INAF, Osservatorio Astrofisico di Arcetri, Largo E. Fermi 5, 50125 Firenze, Italy

<sup>2</sup> IRAM, 300 Rue de la Piscine, F-38406 Saint Martin d'Hères, France

Received date; accepted date

## ABSTRACT

**Context.** In recent years, we have detected clear evidence of rotation in more than 5 hot molecular cores (HMCs). Their identification is confirmed by the fact that the rotation axes are parallel to the axes of the associated bipolar outflows. We have now pursued our investigation by extending the sample to 3 known massive cores, G10.62–0.38, G19.61–0.23, and G29.96–0.02.

**Aims.** We wish to make a thorough study of the structure and kinematics of HMCs and corresponding molecular outflows to reveal possible velocity gradients indicative of rotation of the cores.

**Methods.** We carried out PdBI observations at 2.7 and 1.4 mm of gas and dust with angular resolutions of  $\sim 2''$ – $3''$ , and  $\sim 1''$ – $2''$ , respectively. To trace both rotation and expansion, we simultaneously observed CH<sub>3</sub>CN, a typical HMC tracer, and <sup>13</sup>CO, a typical outflow tracer.

**Results.** The CH<sub>3</sub>CN (12–11) observations have revealed the existence of clear velocity gradients in the three HMCs oriented perpendicular to the direction of the bipolar outflows. For G19 and G29 the molecular outflows have been mapped in <sup>13</sup>CO. The gradients have been interpreted as rotating toroids. The rotation temperatures, used to derive the mass of the cores, have been obtained by means of the rotational diagram method, and lie in the range of 87–244 K. The diameters and masses of the toroids lie in the range of 4550–12600 AU, and 28–415  $M_{\odot}$ , respectively. Given that the dynamical masses are 2 to 30 times smaller than the masses of the cores (if the inclination of the toroids with respect to the plane of the sky is not much smaller than 45°), we suggest that the toroids could be accreting onto the embedded cluster. For G19 and G29, the collapse is also suggested by the redshifted absorption seen in the <sup>13</sup>CO (2–1) line. We infer that infall onto the embedded (proto)stars must proceed with rates of  $\sim 10^{-2} M_{\odot} \text{ yr}^{-1}$ , and on timescales of the order of  $\sim 4 \times 10^3$ – $10^4$  yr. The infall rates derived for G19 and G29 are two orders of magnitude greater than the accretion rates indirectly estimated from the mass loss rate of the corresponding outflows. This suggests that the material in the toroids is not infalling onto a single massive star, responsible for the corresponding molecular outflow, but onto a cluster of stars.

**Key words.** ISM: individual (G10.62–0.38, G19.61–0.23, G29.96–0.02) – ISM: molecules – radio lines: ISM – stars: formation

## 1. Introduction

How do massive ( $> 8 M_{\odot}$ ) stars form? Do they form like lower-mass stars or in a fundamentally different way? What is their connection to star cluster formation? These are crucial questions with profound implications for many areas of astrophysics including high-redshift Population III star formation, galaxy formation and evolution, galactic center environments and super-massive black hole formation, star and star cluster formation, and planet formation around stars in clusters.

In contrast to our fairly mature understanding of isolated low-mass star formation, grasping the details of high-mass star formation has been extremely difficult. High-mass stars are rare objects that form very quickly. What is more, the closest high-mass star forming regions are located further away than the nearest low-mass star form-

ing regions. This, together with the fact that massive stars form in crowded and very obscured regions, implies that the study of the massive star formation process encounters some observational limitations that sometimes cannot be circumvented. Furthermore, the interplay between gravity, turbulence, radiation pressure, ionization and hydromagnetic outflows is also expected to be more complicated in massive star forming region than in low-mass ones. From a theoretical point of view, three-dimensional radiation hydrodynamic simulations by Krumholz et al. (2009) have shown that stars as massive as  $\sim 40 M_{\odot}$  may form through disk accretion and that radiation pressure is not a barrier to form even more massive stars. However, these simulations have also shown that the instabilities that allow accretion to continue lead to fragmentation and the formation of small multiple systems, which could prevent the formation of stars with masses well beyond  $\sim 40 M_{\odot}$ . Therefore, from a theoretical point of view, the formation process of the most massive stars still remains unknown. However, in a very recent work, Kuiper et al. (2010) form stars in excess of  $100 M_{\odot}$  via disk accretion. Nowadays, there are two contending models to explain the formation of massive

Send offprint requests to: M. T. Beltrán, e-mail: mbeltran@arcetri.astro.it

<sup>\*</sup> Based on observations carried out with the IRAM Plateau de Bure Interferometer. IRAM is supported by INSU/CNRS (France), MPG (Germany) and IGN (Spain).

**Table 1.** Phase centers, distances, luminosities, and LSR velocities of the sources

Core	IRAS PSC name	Position <sup>a</sup>		$L_{\text{bol}}^b$ ( $L_{\odot}$ )	$V_{\text{LSR}}$ ( $\text{km s}^{-1}$ )	$d$ (kpc)	Refs. <sup>c</sup>
		$\alpha(\text{J2000})$ h m s	$\delta(\text{J2000})$ ° ' "				
G10.62–0.38	18075–1956	18 10 28.650	–19 55 49.50	$0.4 \times 10^6$	–2.0	3.4	1
G19.61–0.23	18248–1158	18 27 38.145	–11 56 38.49	$2.2 \times 10^6$	41.6	12.6	2
G29.96–0.02	18434–0242	18 46 03.955	–02 39 21.87	$3.2 \times 10^5$	98.9	3.5	3

<sup>a</sup> Coordinates of the phase center of the observations.

<sup>b</sup> The bolometric luminosities were calculated by integrating the IRAS flux densities. The contribution from longer wavelengths was taken into account by extrapolating according to a black-body function that peaks at  $100 \mu\text{m}$  and has the same flux density as the source at this wavelength.

<sup>c</sup> References for the distances: 1: Blum et al. (2001); 2: Kolpak et al. (2003); 3: L. Moscadelli (2010, private communication)

stars: the core accretion model (McKee & Tan 2002; 2003), and the competitive accretion model (Bonnell et al. 2007). In the core accretion model, a massive star forms from a massive core which was fragmented from the natal molecular cloud, and gather its mass from this massive core only. Given the non-zero angular momentum of the collapsing core, this models predicts the existence of protostellar accretion disks around massive stars. What is more, due to the high density in massive cores, the accretion rate onto these disks is extremely high. On the other hand, in the competitive accretion model, a molecular cloud initially fragments in mainly low-mass cores, which form stars which compete to accrete mass from the common reservoir of gas. Therefore, massive stars should form exclusively in clustered environments. In this scenario, the circumstellar environment is strongly perturbed and any circumstellar disk could be severely affected and possibly truncated by interactions with stellar companions.

In recent years, a few Keplerian circumstellar disks and massive rotating toroids around respectively newly born B- and O-type stars have been detected (see review by Cesaroni et al. 2007 and references therein). In particular, our group has detected a few rotating structures by searching for velocity gradients perpendicular to molecular outflows powered by massive young stellar objects (e.g. Cesaroni et al. 1999; Beltrán et al. 2004; 2005; Furuya et al. 2008). However, notwithstanding these important results, the controversy on massive star formation is still open (see Beuther et al. 2007a and Bonnell et al. 2007). To pursue our investigation and establish that the disk/toroid phenomenon is a common product of massive star formation, we have extended the sample to a larger number of objects. On the basis of previous experience,  $\text{CH}_3\text{CN}$  has been used as disk/toroid tracer. Note that Arce et al. (2008) and Codella et al. (2009) have reported the detection of  $\text{CH}_3\text{CN}$  tracing bow shocks in the low-mass L1157-B1 molecular outflow clumps. However, in L1157, the emission is detected far from the core harboring the embedded protostar and clearly not associated with it, and what is more, the column densities estimated towards the L1157-B1 clumps (Codella et al. 2009) are 3–4 orders of magnitude smaller than those estimated towards rotating toroids (Beltrán et al. 2005). In this study, we have used  $^{13}\text{CO}$  as molecular outflow tracer. As mentioned above, the presence of molecular outflows has proved to be very valuable as indirect evidence for the presence of a disk: all accretion scenarios predict the molecular outflows to be orientated perpendicular to the accretion disks. In crowded regions, this simple picture of perpendicularity can be more complicated due to interac-

tions among different molecular outflows from young stellar objects (YSOs) in the core. Therefore, when searching for rotating structures it is very crucial to properly constrain though high-angular resolution observations the geometry and orientation of the molecular outflows. The results of this study are presented here.

## 2. The sample

We have chosen well known hot molecular cores (HMCs), whose kinematics has been studied in previous interferometric observations, revealing velocity gradients in the cores, which are suggestive of rotation, and evidence of outflows. Two of them lie close to an UC HII region, and one of them contains an embedded UC HII region.

*G10.62–0.38*: The G10.62–0.38 (hereafter G10) core, located at a distance of 3.4 kpc (Blum et al. 2001) contains a well-studied UC HII region (e.g. Wood & Churchwell 1989) associated with the infrared source IRAS 18075–1956. G10 is embedded in a HMC that has been extensively mapped in  $\text{NH}_3$  (Ho & Haschick 1986; Keto et al. 1987, 1988; Sollins et al. 2005), and more recently in  $\text{SO}_2$  and  $\text{OCS}$  (Klaassen et al. 2009). In these studies, infall and bulk rotation in the molecular gas surrounding the UC HII region have been detected. In addition, recent  $\text{H66}\alpha$  observations have shown that inward motions are also detected in the ionized gas (Keto 2002), suggesting the existence of an ionized accretion flow.  $\text{CH}_3\text{OH}$  and  $\text{H}_2\text{O}$  masers have been mapped towards the core and are distributed linearly in the plane of the rotation (Hofner & Churchwell 1996; Walsh et al. 1998), while OH masers seem to lie along the axis of rotation (Argon et al. 2000). The presence of a molecular outflow with a P.A. of  $\sim 45^\circ$  has been first suggested by Keto & Wood (2006), who present a position-velocity diagram of the high-velocity ionized jet, and Klaassen et al. (2009), but no high-angular resolution outflow maps are available yet. On the other hand, López-Sepulcre et al. (2009) have used the IRAM 30-m telescope to map the molecular outflow in the  $^{13}\text{CO}$  (2–1) line, which shows a direction consistent with that proposed by Keto & Wood (2006).

*G19.61–0.23*: The G19.61–0.23 core (hereafter G19), located at a distance of 12.6 kpc (Kolpak et al. 2003), is an extremely complex site associated with the infrared source IRAS 18248–1158. The core contains a group of embedded UC HII regions, firstly detected by Garay et al. (1985), and more recently mapped by Furuya et al. (2005). The G19 HMC has been mapped in several molecular tracers, such as  $\text{CS}$ ,  $\text{NH}_3$ ,  $\text{CH}_3\text{CH}_2\text{CN}$ ,  $\text{HCOOCH}_3$ , and  $\text{CH}_3\text{CN}$  (Plume et al. 1992; Garay et al 1998; Remijan et al. 2004;

**Table 2.** Parameters of the IRAM PdBI observations

Source	Configuration <sup>a</sup>	Wavelength (mm)	Synthesized beam <sup>b</sup> (arcsec)	P.A. (deg)
G10	B	2.7	$3.6 \times 1.6$	-167
		1.4	$2.4 \times 0.7$	-169
G19	C	2.7	$4.1 \times 1.8$	-161
		1.4	$2.6 \times 1.0$	-161
G29	A,C	2.7	$2.7 \times 1.3$	-168
		1.4	$1.4 \times 0.7$	-168

<sup>a</sup> Note that the A, B, and C configurations of years 2004 and 2005 are different from the corresponding nowadays configurations.

<sup>b</sup> The synthesized CLEANed beams for maps made using natural weighting.

**Table 3.** Frequency setups used for the molecular lines observed with the IRAM PdBI

Line	Center frequency (MHz)	Bandwidth (MHz)	Spectral resolution (MHz) (km s <sup>-1</sup> )	
CH <sub>3</sub> CN (6-5), CH <sub>3</sub> <sup>13</sup> CN (6-5)	110383.508	80	0.156	0.4 <sup>a</sup>
CH <sub>3</sub> CN (6-5), CH <sub>3</sub> <sup>13</sup> CN (6-5)	110383.508	320	2.5	6.9
CH <sub>3</sub> <sup>13</sup> CN (6-5), <sup>13</sup> CO (1-0)	110320.430	160	0.625	1.7
CH <sub>3</sub> CN (6-5) $v_8 = 1$	110609.550	160	0.625	1.7
CH <sub>3</sub> CN (12-11)	220747.266	80	0.156	0.2 <sup>a</sup>
CH <sub>3</sub> CN (12-11), CH <sub>3</sub> <sup>13</sup> CN (12-11)	220679.297	80	0.156	0.2 <sup>a</sup>
CH <sub>3</sub> CN (12-11), CH <sub>3</sub> <sup>13</sup> CN (12-11)	220594.422	160	0.625	0.9 <sup>b</sup>
CH <sub>3</sub> CN (12-11), CH <sub>3</sub> <sup>13</sup> CN (12-11), <sup>13</sup> CO (2-1)	220475.812	320	2.5	3.4

<sup>a</sup> The spectral resolution in the maps has been degraded to 0.5 km s<sup>-1</sup>.

<sup>b</sup> The spectral resolution in the maps has been degraded to 1.0 km s<sup>-1</sup>.

Furuya et al. 2005; Wu et al. 2009). Inverse P-Cygni profiles have been detected in <sup>13</sup>CO, C<sup>18</sup>O, and CN towards the core (Wu et al. 2009; Furuya et al. 2010), which indicate gas infalling towards the center. A molecular outflow has been mapped towards the core through <sup>13</sup>CO single-dish observations (López-Sepulcre et al. 2009), but its direction is not well defined. Masers of H<sub>2</sub>O, OH, and CH<sub>3</sub>OH have also been detected in this core (Forster & Caswell 1989; Hofner & Churchwell 1996; Walsh et al. 1998).

*G29.96-0.02*: The G29.96-0.02 core (hereafter G29), located at a distance of 3.5 kpc (L. Moscadelli, 2010, private communication) and associated with the infrared source IRAS 18434-0242, contains a well-studied cometary UC HII region (e.g. Cesaroni et al. 1994; De Buizer et al. 2002) with a HMC located right in front of the cometary arc (e.g. Wood & Churchwell 1989; Cesaroni et al. 1994, 1998). The HMC has been mapped in several tracers, such as NH<sub>3</sub>, HCO<sup>+</sup>, CS, CH<sub>3</sub>CN, HNCO, HCOOCH<sub>3</sub> (Cesaroni et al. 1998; Pratap et al. 1999; Maxia et al. 2001; Olmi et al. 2003; Beuther et al. 2007b). Cesaroni et al. (1998) and Olmi et al. (2003) have detected in NH<sub>3</sub> and CH<sub>3</sub>CN a velocity gradient across the HMC approximately along the east-west direction, interpreted as rotation. This is similar to the velocity gradient observed in HN<sup>13</sup>C by Beuther et al. (2007b). A molecular outflow in the southeast-northwest direction and centered on the HMC has been mapped in H<sub>2</sub>S by Gibb et al. (2004). The same outflow has been mapped in SiO (8-7) by Beuther et al. (2007b). Masers of H<sub>2</sub>O, CH<sub>3</sub>OH, and H<sub>2</sub>CO have also been detected towards the HMC (Hofner & Churchwell 1996; Walsh et al. 1998; Hoffman et al. 2003).

### 3. Observations

Interferometric observations of G10, G19, and G29 were carried out with the IRAM Plateau de Bure Interferometer

(PdBI) on February 28 and March 16, 2004, and on February 26 and March 21, 2005. G29 was observed in the most extended and compact configurations, A and C, respectively, while cores G19 and G10 were observed in the extended and compact ones, B and C, respectively. Due to technical problems during the observations, for G19 the only usable configuration was the compact one, while for G10 the only usable configuration was the extended one. Table 2 reports the configurations used for each source and the synthesized beams. By using the dual frequency capabilities of the PdBI we observed simultaneously at 2.7 and 1.4 mm. The frequency setup of the correlator and the list of the observed molecular lines are shown in Table 3. The units of the correlator were placed in such a way that a frequency range free of lines could be used to measure the continuum flux. The phase centers used are indicated in Table 1. The bandpass of the receivers was calibrated by observations of the quasar 3C273. Amplitude and phase calibrations were achieved by monitoring 1730-130 and 1741-038, whose flux densities were determined relative to MWC349 or 1749+096. The flux densities estimated for 1730-130 are in the range 1.55-2.41 Jy at 2.7 mm, and 0.78-1.71 Jy at 1.4 mm, while those for 1741-038 are in the range 3.57-3.80 Jy at 2.7 mm, and 2.18-2.77 Jy at 1.4 mm. The uncertainty in the amplitude calibration is estimated to be ~20%. The data were calibrated and analyzed with the GILDAS<sup>1</sup> software package developed at IRAM and Observatoire de Grenoble. The continuum maps were created from the line free channels. We subtracted the continuum from the line emission directly in the (*u,v*)-domain.

<sup>1</sup> The GILDAS package is available at <http://www.iram.fr/IRAMFR/GILDAS>

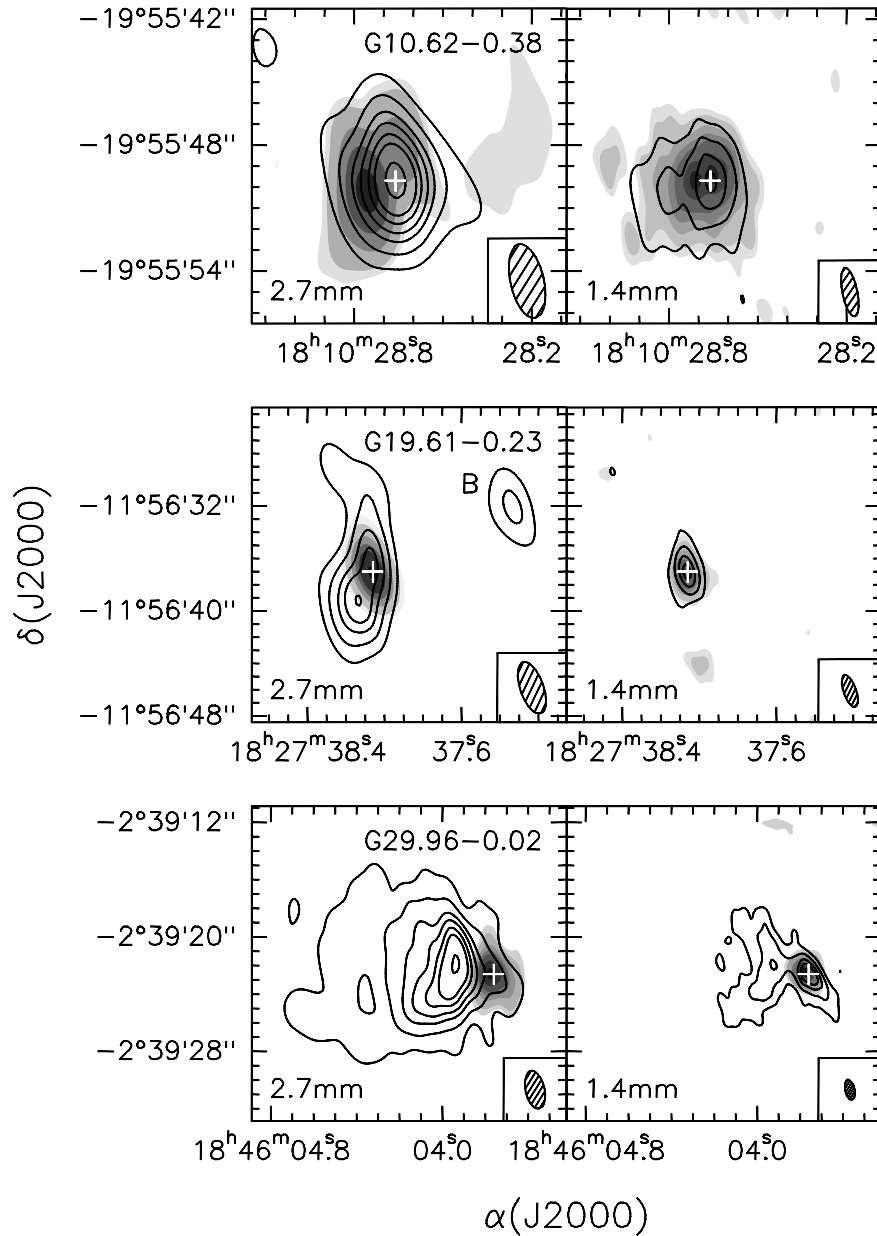


**Fig. 1.** Overlay of the PdBI maps of the 2.7 mm (*left panels*) and the 1.4 mm (*right panels*) continuum emission (*contours*) on the CH<sub>3</sub>CN (6–5) emission (*greyscale*) averaged under the  $K = 0, 1, 2, 3,$  and 4 components (*left panels*) and CH<sub>3</sub>CN (12–11) emission (*greyscale*) averaged under the  $K = 0, 1, 2,$  and 3 components (*right panels*) towards the cores G10.62–0.38, G19.61–0.23, and G29.96–0.02. The contour levels are 3, 9, 18, 27, 39, 51, and 75 times  $\sigma$ , where  $1\sigma$  is  $17 \text{ mJy beam}^{-1}$  and  $26.7 \text{ mJy beam}^{-1}$  at 2.7 and 1.4 mm, respectively, for G10.62–0.38,  $6 \text{ mJy beam}^{-1}$  and  $33.3 \text{ mJy beam}^{-1}$  at 2.7 and 1.4 mm, respectively, for G19.61–0.23, and  $3 \text{ mJy beam}^{-1}$  and  $6.7 \text{ mJy beam}^{-1}$  at 2.7 and 1.4 mm, respectively, for G29.96–0.02. Greyscale levels are 3, 5, 10, 15, 20, 30, and 40 times (36 for G10)  $\sigma$ , where  $1\sigma$  is  $15 \text{ mJy beam}^{-1}$  at 2.7 mm and  $15 \text{ mJy beam}^{-1}$  at 1.4 mm for G10,  $30 \text{ mJy beam}^{-1}$  at 2.7 mm and  $50 \text{ mJy beam}^{-1}$  at 1.4 mm for G19, and  $15 \text{ mJy beam}^{-1}$  at 2.7 mm and  $65 \text{ mJy beam}^{-1}$  at 1.4 mm for G29. The synthesized beam is shown in the lower right-hand corner. The white cross marks the position of the 1.4 mm continuum emission peak. The source B seen towards G19.61–0.23 at 2.7 mm is the UC HII region B observed by Furuya et al. (2005).

## 4. Results

### 4.1. Continuum emission

Figure 1 shows the PdBI maps of the 2.7 and 1.4 mm continuum emission overlaid on the CH<sub>3</sub>CN (6–5) and CH<sub>3</sub>CN (12–11) emission towards the three cores. The position and fluxes at 2.7 and 1.4 mm, and the deconvolved size of the sources, measured as the average diameter of the 50% con-

tour at 1.4 mm, are given in Table 4. As seen below, the millimeter emission at 2.7 mm of the cores is highly contaminated by free-free emission of the nearby or embedded UC HII region(s). Due to the fact that the 1.4 mm emission is less affected by this problem and traces better the HMC, the positions given in Table 4 are those of the 1.4 mm emission peak.

**Table 4.** Positions, flux densities, and diameters of the cores

Core	Position <sup>a</sup>		2.7 mm			1.4 mm			Source Diameter <sup>d</sup>	
	$\alpha$ (J2000)	$\delta$ (J2000)	$I_{\nu}^{\text{peak}}$	TOTAL <sup>b</sup>	HMC <sup>c</sup>	$I_{\nu}^{\text{peak}}$	TOTAL <sup>b</sup>	HMC <sup>c</sup>	$\theta_s$	$\theta_s$
	h m s	° ' "	(Jy/beam)	(Jy)	(Jy)	(Jy/beam)	(Jy)	(Jy)	(arcsec)	(AU)
G10	18 10 28.66	−19 55 49.7	1.44	2.42	0.28	0.77	3.40	1.40	2.0	6800
G19 <sup>e</sup>	18 27 38.06	−11 56 37.0	0.24	0.64	0.16	1.02	1.50	1.50	1.0	12600
G19B <sup>f</sup>	18 27 37.33	−11 56 32.1	0.07	0.07	...	... <sup>g</sup>	... <sup>g</sup>	... <sup>g</sup>	... <sup>g</sup>	... <sup>g</sup>
G29	18 46 03.76	−02 39 22.6	0.31	2.00	...	0.26	2.03	0.83	1.3	4550

<sup>a</sup> Position of the 1.4 mm emission peak.

<sup>b</sup> The total (free-free and dust) flux density.

<sup>c</sup> Flux density of the Hot Molecular Core. See Sect. 4.1 for a description of how the HMC flux density has been calculated.

<sup>d</sup> Deconvolved average diameter of the 50% contour at 1.4 mm.

<sup>e</sup> The flux at 2.7 mm includes the emission of the UC HII regions A, C, D, F, and J (Furuya et al. 2005).

<sup>f</sup> Position and flux density at 2.7 mm of the UC HII region B (Furuya et al. 2005).

<sup>g</sup> Source not detected at 1.4 mm. Position corresponds to the 2.7 mm emission peak.

#### 4.1.1. G10.62–0.38

The continuum dust emission of G10, which is hardly resolved at 2.7 mm, shows a compact source plus an extended envelope. The peak of the emission at 1.4 mm coincides with that at 2.7 mm, and is very close to the position of the UC HII region (see Fig. 1 of Sollins et al. 2005). As seen in Fig. 1, the continuum emission at 1.4 mm coincides with the CH<sub>3</sub>CN (12–11) emission. At this wavelength, the source is clearly resolved in the east-west direction, and shows an eastern elongation, associated with CH<sub>3</sub>CN emission, which suggests the presence of another embedded source. On the other hand, at 2.7 mm, the peak of the continuum emission is slightly displaced from the peak of the CH<sub>3</sub>CN (6–5) averaged emission. Although we cannot rule out the possibility of the existence of another embedded eastern source, the displacement of the line emission is likely due to the fact that the observations of this core have been carried out only with the extended configuration. Therefore, part of the extended line emission has been filtered out by the interferometer, making it very difficult to properly clean the dirty line maps.

To derive a rough estimate of the free-free contribution of the UC HII region at millimeter wavelengths, we have extrapolated the 1.3 cm emission measured by Sollins & Ho (2005) assuming optically thin free-free emission ( $S_{\nu} \propto \nu^{-0.1}$ ). The flux integrated density at 1.3 cm is 2.5 Jy, and the expected free-free emission is  $\sim 2.14$  and  $\sim 2.00$  Jy at 2.7 and 1.4 mm, respectively. Therefore, the dust continuum emission associated with the HMC is 0.28 and 1.40 Jy at 2.7 and 1.4 mm, respectively (see table 4). Klaassen et al. (2009) have estimated a thermal dust emission of 2 Jy at 1.4 mm. However, the free-free emission contribution at 1.4 mm estimated by these authors from radio recombination lines, is less than half (0.92 Jy; P. D. Klaassen 2010, private communication) our estimate. The spectral index of the dust emission between 2.7 and 1.4 mm is 2.3, which corresponds to a power-law index  $\beta$  of the dust emissivity of 0.3. This value of  $\beta$  is very low and indicates that the contribution of the free-free emission at 2.7 mm is likely higher than estimated. Therefore,  $\beta$  should be taken as a lower limit.

#### 4.1.2. G19.61–0.23

The continuum dust emission of G19 at 2.7 mm is clearly different from that at 1.4 mm. The emission at 2.7 mm is dominated by the free-free emission of the UC HII regions embedded in the core (e.g. Furuya et al. 2005). As seen in Fig. 1, the emission shows two clumps: the eastern and larger one associated with the UC HII regions A, C, D, F, and J, with a morphology similar to the one mapped at 3.5 cm by Furuya et al. (2005); and the western and smaller one associated with the UC HII region B. The position and flux density of this source at 2.7 mm are reported in Table 4. On the other hand, the emission at 1.4 mm is clearly associated with the HMC, traced by the CH<sub>3</sub>CN (12–11) line emission. The HMC is also visible in CH<sub>3</sub>CN (6–5) at 2.7 mm. This dichotomy between the emission at 2.7 and 1.4 mm is also reflected in the position of the peak, which at 2.7 mm ( $\alpha$ (J2000) = 18<sup>h</sup> 27<sup>m</sup> 38<sup>s</sup>.13,  $\delta$ (J2000) = −11° 56′ 39″.3) does not coincide with that at 1.4 mm (see Table 4).

Due to the complexity of the free-free emission and the number of UC HII regions embedded in the eastern core at 2.7 mm, it is very difficult to estimate the free-free emission contribution at millimeter wavelengths by extrapolating the centimeter emission. Instead, we have estimated the dust continuum emission of the HMC by measuring the flux density in a region surrounding the HMC as traced by the CH<sub>3</sub>CN (6–5) line. The flux density at 2.7 mm is  $\sim 160$  mJy, which is a value consistent with the 147 mJy measured by Furuya et al. (2005) at 3.3 mm. At 1.4 mm, the emission seems to be associated only with the HMC, and therefore, we have assumed that the continuum emission is thermal dust (see Table 4). The spectral index of the HMC between 2.7 and 1.4 mm is 3.2, which corresponds to  $\beta=1.2$ . Furuya et al. (2010) have estimated  $\beta \gtrsim 0.7$  between 3 mm and 890  $\mu\text{m}$ , a value lower but still consistent with our estimate.

#### 4.1.3. G29.96–0.02

Alike the case of G19, also in G29 the 2.7 mm continuum emission towards the core is different from that at 1.4 mm. At 2.7 mm, the emission is clearly contaminated by the cometary UC HII region and outlines the cometary arc seen in previous observations at centimeter (e.g. Cesaroni

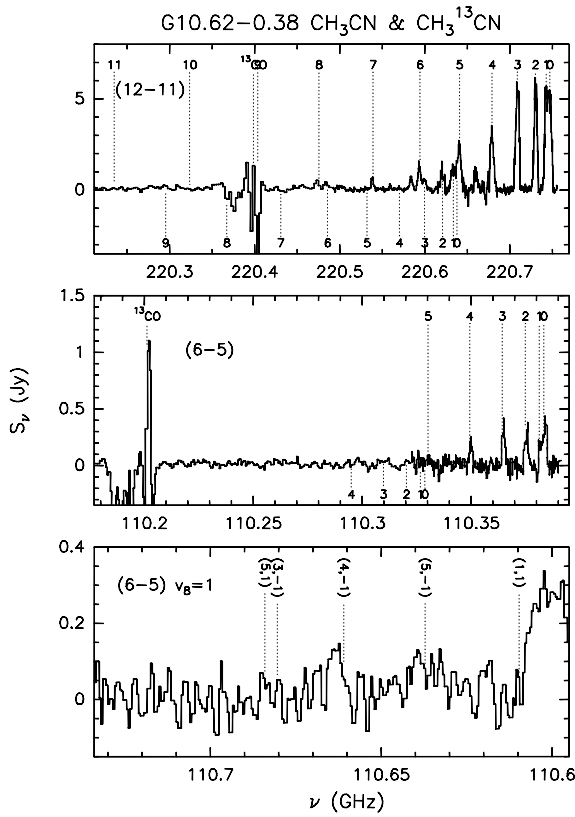


**Fig. 2.** Methyl cyanide spectra obtained by integrating the emission inside the  $3\sigma$  contour level area at 2.7 and 1.4 mm towards G10 as seen with the PdBI. We show in the top  $\text{CH}_3\text{CN}$  (12–11), in the middle  $\text{CH}_3\text{CN}$  (6–5), and in the bottom  $\text{CH}_3\text{CN}$  (6–5) vibrationally excited ( $v_8 = 1$ ). The different  $K$ -components (*top* and *middle* panels) are marked with dashed lines in the upper (lower) part of each spectra in the case of  $\text{CH}_3\text{CN}$  ( $\text{CH}_3^{13}\text{CN}$ ). Note that different  $K$ -components of a same transition may have different spectral resolution because they were observed with different correlator units. Labeled only the analyzed lines.

et al. 1994) and mid-infrared wavelengths (De Buizer et al. 2002). Some emission is also visible in front of the arc, associated with the HMC traced by the  $\text{CH}_3\text{CN}$  (6–5) line and  $\text{H}_2\text{O}$  maser emission (Hofner et al. 1996; Olmi et al. 2003). At 1.4 mm, the cometary arc is still visible, but the strongest continuum emission is associated with the HMC traced by the  $\text{CH}_3\text{CN}$  (12–11) line emission in front of the arc. In fact, the peak at 2.7 mm ( $\alpha(\text{J2000}) = 18^{\text{h}} 46^{\text{m}} 03^{\text{s}}.94$ ,  $\delta(\text{J2000}) = -02^{\circ} 39' 21''.9$ ) is shifted by  $2''.7$  eastwards with respect to that at 1.4 mm (Table 4).

To obtain a rough estimate of the free-free contribution to the 2.7 mm continuum emission, we have extrapolated the 1.3 cm emission measured by Cesaroni et al. (1994) to 2.7 mm assuming optically thin free-free emission. We have measured the flux density at 1.3 cm inside a region that corresponds to the  $3\sigma$  contour level of the 2.7 mm continuum emission and obtained a value of 2.74 Jy. Therefore, the expected free-free emission at 2.7 mm is  $\sim 2.35$  Jy. This value is higher than the flux density measured at 2.7 mm (see Table 4). Given the fact that the uv-coverages of the centimeter and millimeter observations are different, it is not surprising that the expected free-free emission value is higher than that actually measured. It is evident that

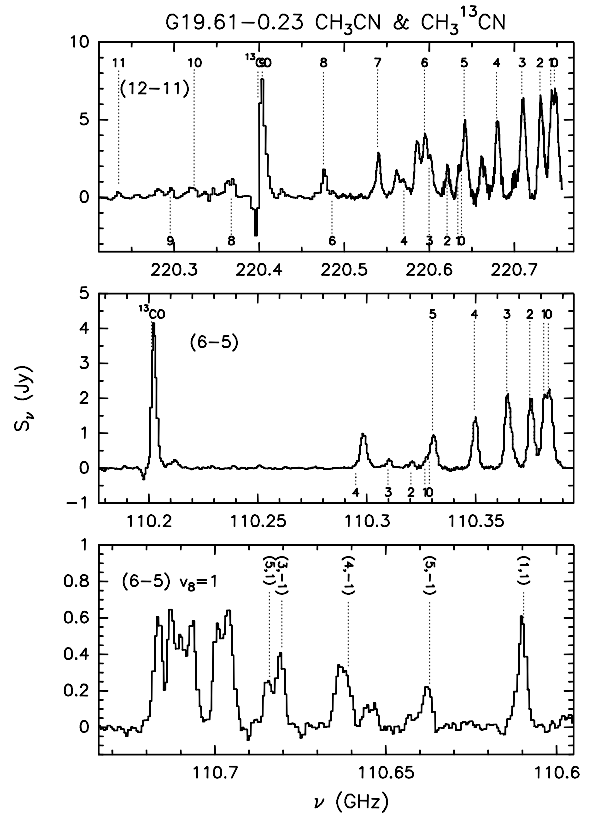


**Fig. 3.** Same as Fig. 2 for G19.

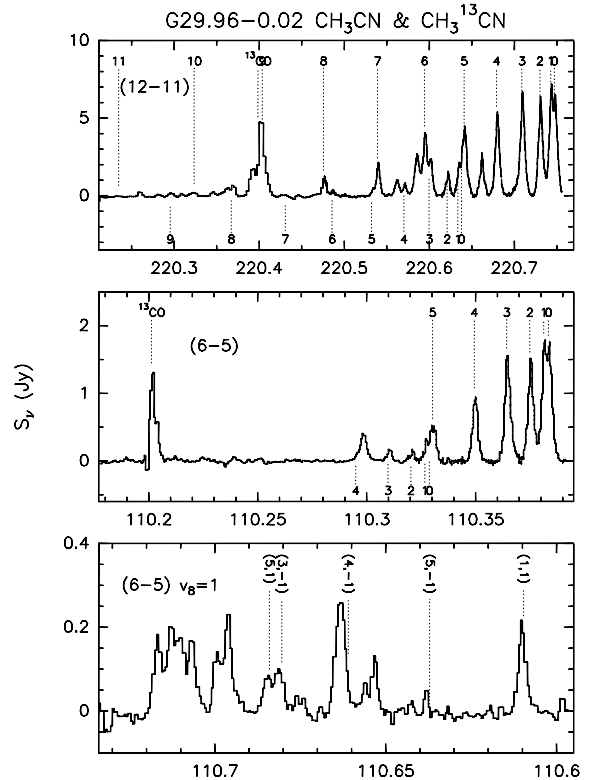


**Fig. 4.** Same as Fig. 2 for G29.

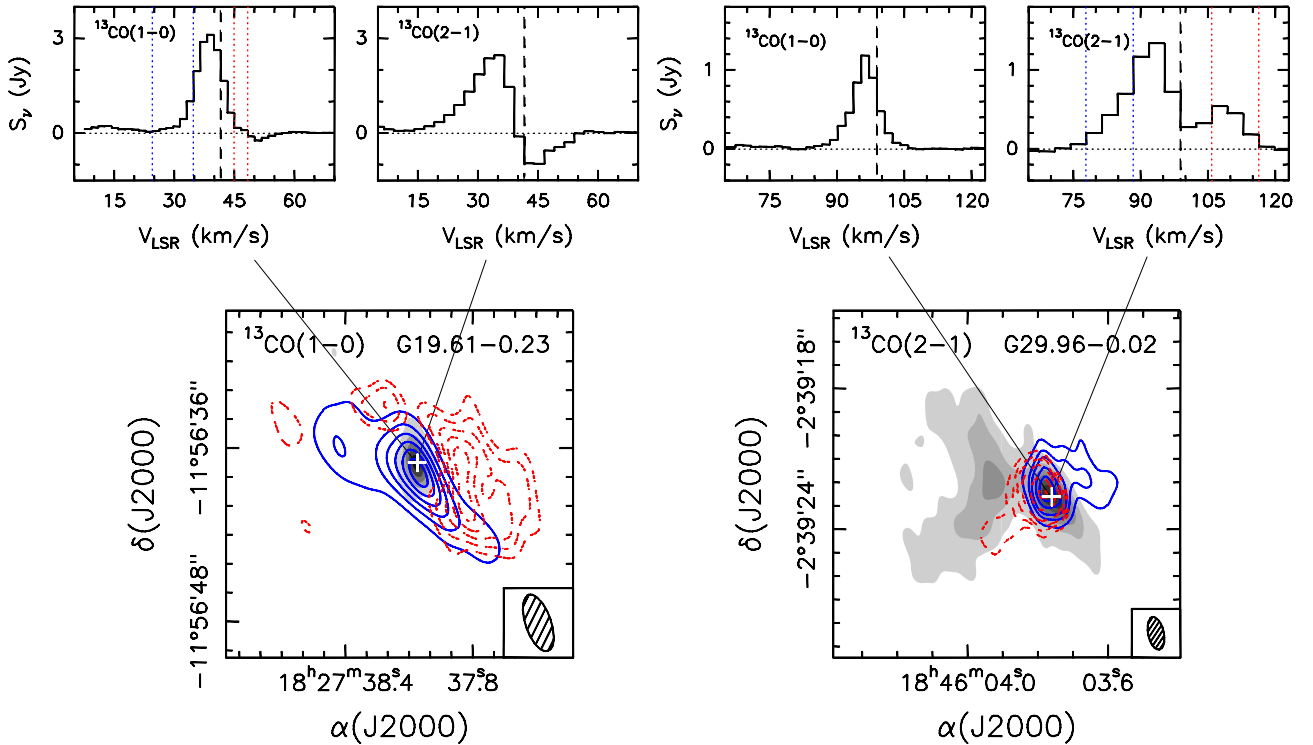


**Fig. 5.** *Bottom panels:* Blueshifted (*blue solid contours*) and redshifted (*red dashed contours*)  $^{13}\text{CO}$  (1–0) (*left*) and  $^{13}\text{CO}$  (2–1) (*right*) averaged emission overlaid on the 1.4 mm continuum emission (*greyscale*) towards G19 and G29, respectively. The velocity intervals for which the blueshifted and redshifted emission have been averaged are indicated in blue and red dotted vertical lines in the corresponding upper spectra. Contour levels are 0.05, 0.1, 0.15, 0.2, 0.25, 0.3, and 0.35  $\text{Jy beam}^{-1}$  ( $1\sigma \simeq 7 \text{ mJy beam}^{-1}$ ) for the  $^{13}\text{CO}$  (1–0) blueshifted emission and 0.15, 0.2, 0.25, 0.3, and 0.35  $\text{Jy beam}^{-1}$  ( $1\sigma \simeq 50 \text{ mJy beam}^{-1}$ ) for the  $^{13}\text{CO}$  (1–0) redshifted emission (G19), and 0.03, 0.09, 0.15, 0.27, 0.39, and 0.51  $\text{Jy beam}^{-1}$  ( $1\sigma \simeq 7 \text{ mJy beam}^{-1}$ ) for the  $^{13}\text{CO}$  (2–1) blueshifted emission and 0.03, 0.06, 0.09, 0.15, 0.3 and 0.45  $\text{Jy beam}^{-1}$  ( $1\sigma \simeq 7 \text{ mJy beam}^{-1}$ ) for the  $^{13}\text{CO}$  (2–1) redshifted emission (G29). Greyscale contours for the continuum emission are the same as in Fig. 1. The synthesized beam is shown in the lower right-hand corner. The white cross marks the position of the 1.4 mm continuum emission peak. *Top panels:*  $^{13}\text{CO}$  (1–0) and (2–1) spectra taken towards the 1.4 mm continuum emission peak of the G19 (*left*) and G29 (*right*) cores. The dashed vertical line indicates the systemic velocity of each core.

the emission at this wavelength is dominated by free-free emission. According to Olmi et al. (2003), who have estimated the contribution of the free-free emission at 2.7 mm by using the same uv-coverage and restoring beam at centimeter and millimeter wavelengths, the expected thermal dust contribution is  $\sim 0.15 \text{ Jy}$ . Using the same method, Maxia et al. (2001) estimated a dust emission of 0.24 Jy at 3.4 mm, which shows the uncertainty of these measurements. At 1.4 mm, the emission from the HMC is clearly distinguishable from that of the cometary arc associated with the UC HII region. Therefore, the continuum dust emission of the HMC has been estimated by measuring the flux density in a region surrounding it. The flux density of 0.83 Jy is slightly higher than the value of 0.56 Jy estimated at 1.3 mm by Maxia et al. (2001) after subtracting the free-free contribution. Maxia et al. (2001) mention that their flux density measurement at 1.3 mm is lower than expected, and could be affected by spatial filtering of extended emission. Adopting the values of Olmi et al. (2003) at 2.7 mm and our estimate at 1.4 mm, one obtains a spectral index of 2.5, which corresponds to  $\beta=0.5$ . This value of  $\beta$  is very low and indicates that the contribution of the free-free emission at 2.7 mm is likely higher than estimated. Therefore,  $\beta$  should be taken as a lower limit.

#### 4.2. $\text{CH}_3\text{CN}$

Maps of the  $\text{CH}_3\text{CN}$  (6–5) emission averaged under the  $K = 0, 1, 2, 3,$  and 4 components, and  $\text{CH}_3\text{CN}$  (12–11) emission averaged under the  $K = 0, 1, 2,$  and 3 components towards G10, G19, and G29 are shown in Fig. 1. Figures 2, 3, and 4 show the spectra of the  $\text{CH}_3\text{CN}$  and  $\text{CH}_3^{13}\text{CN}$  (12–11) and (6–5) lines towards the three cores. The first vibrational state above the ground of the  $\text{CH}_3\text{CN}$  (6–5) line, which is denoted as  $v_8 = 1$ , is also shown in the figures. The spectra have been obtained by averaging the emission inside the  $3\sigma$  contour levels of the corresponding maps in Fig. 1.

Several  $K$ -components of the different rotational transitions of  $\text{CH}_3\text{CN}$  and  $\text{CH}_3^{13}\text{CN}$  at 1.4 and 2.7 mm are clearly detected towards the cores. Towards G10, only the  $K = 0-4$  components of  $\text{CH}_3\text{CN}$  (6–5) are visible. Several lines of  $\text{CH}_3\text{CN}$  (6–5)  $v_8 = 1$  are also clearly detected towards G19 and G29 (Fig. 2), whereas towards G10, only few weak  $\text{CH}_3\text{CN}$  (6–5)  $v_8 = 1$  lines are visible. As already mentioned in Sect. 4.1.1, the line emission of G10 at 2.7 mm could be severely affected by the fact that the extended emission is resolved out.

As seen in Fig. 1, the  $\text{CH}_3\text{CN}$  (12–11) emission is barely resolved in G19 and G29, and peaks at the same position as the 1.4 mm continuum emission. On the other hand, in

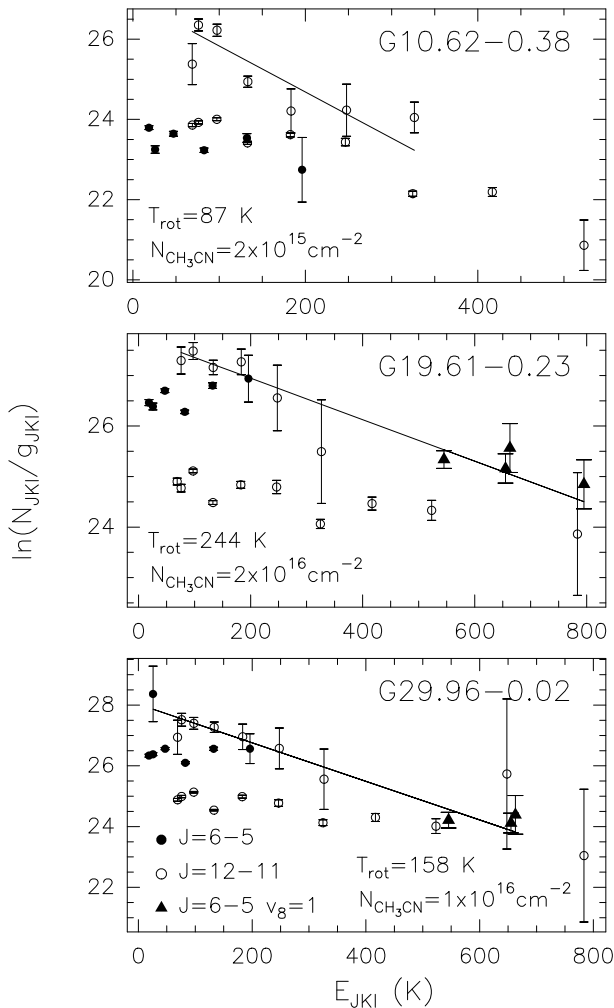


**Fig. 6.** Rotation diagram for G10, G19, and G29 with superimposed fit. Only the data for the  $\text{CH}_3^{13}\text{CN}$  transitions and the  $\text{CH}_3\text{CN}$  (6–5)  $v_8 = 1$  transition have been fitted. Filled circles, open circles, and filled triangles correspond to the  $\text{CH}_3^{13}\text{CN}$  (6–5), the  $\text{CH}_3^{13}\text{CN}$  (12–11), and the  $\text{CH}_3\text{CN}$  (6–5)  $v_8 = 1$  transition, respectively.

G10, the  $\text{CH}_3\text{CN}$  (12–11) emission is clearly resolved and shows two peaks: a western one associated with the 1.4 mm continuum emission peak plus a weaker one to the east.

#### 4.3. $^{13}\text{CO}$

We have clearly detected the  $^{13}\text{CO}$  (1–0) and (2–1) lines towards the cores (see Figs. 2, 3, and 4). In G10, the line profiles exhibit a strong lack of emission at the center, probably due to a missing flux problem since the interferometer has filtered out part of the extended emission. Therefore, for this core the  $^{13}\text{CO}$  emission has not been analyzed.

Figure 5 shows the  $^{13}\text{CO}$  (1–0) and (2–1) spectra at the 1.4 mm continuum emission peak in G19 and G29. As seen in this figure, the  $^{13}\text{CO}$  spectra for these two cores are also affected by lack of emission at the central velocities. Although, we cannot exclude the possibility that the lack of emission is due to a missing flux problem, the fact that it is observed at redshifted velocities suggests that it could be due to absorption. This possibility will be discussed in

Sects. 5.3.2 and 5.3.3. In the bottom panels of Fig. 5, we present the maps of the  $^{13}\text{CO}$  (1–0) averaged blueshifted and redshifted emission with respect to the systemic velocity of G19 (41.6 km s $^{-1}$ ) and of the  $^{13}\text{CO}$  (2–1) averaged blueshifted and redshifted emission with respect to the systemic velocity of G29 (98.9 km s $^{-1}$ ) overlaid on the 1.4 mm continuum emission of each core. The  $^{13}\text{CO}$  emission traces a molecular outflow in each core: one oriented east-west in G19, and one oriented southeast-northwest in G29. The latter one had been previously mapped in  $\text{H}_2\text{S}$  and  $\text{SiO}$  by Gibb et al. (2004) and Beuther et al. (2007b), respectively. Taking into account the blueshifted and redshifted emission, the total extent of the outflows is  $\sim 14''$  ( $\sim 0.86$  pc) in G19, and  $\sim 6''$  ( $\sim 0.10$  pc) in G29.

## 5. Discussion

### 5.1. Temperature and mass estimates

$\text{CH}_3\text{CN}$  is a symmetric top molecule, and therefore, can be used to estimate the temperature in the cores. The rotational temperature,  $T_{\text{rot}}$ , and the total methyl cyanide column density,  $N_{\text{CH}_3\text{CN}}$ , can be estimated by means of the rotation diagram method, which assumes that the molecular levels are populated according to LTE conditions at a single temperature  $T_{\text{rot}}$ . In the high density limit where level populations are thermalized, one expects that  $T_{\text{rot}} = T_{\text{kin}}$ , the kinetic temperature. The  $\text{CH}_3\text{CN}$  ground level transitions appear to be optically thick for all cores, as suggested by the ratio between the main species and isotopomer. Therefore, although in the Boltzmann plot we show all the measurements (see Fig. 6), the fit was performed only using the  $\text{CH}_3^{13}\text{CN}$  and vibrational excited  $\text{CH}_3\text{CN}$  transitions. All the spectra were obtained by averaging the emission inside the  $3\sigma$  contour levels of the corresponding maps in Fig. 1. The values obtained at 1.4 mm were afterwards corrected to take into account the smaller area used to average the emission as compared to the 2.7 mm emission. The relative abundances  $[\text{CH}_3\text{CN}]/[\text{CH}_3^{13}\text{CN}]$  were estimated following Wilson & Rood (1994), who give interstellar abundances as a function of Galactocentric distance, and are 47, 44, and 50 for G10, G19, and G29, respectively.

Figure 6 shows the rotational diagram together with the fits and the estimated  $T_{\text{rot}}$  and  $N_{\text{CH}_3\text{CN}}$  for each core. The rotational temperatures obtained with the fits are 87, 244, and 158 K for G10, G19, and G29, respectively, while  $N_{\text{CH}_3\text{CN}}$  are  $2 \times 10^{15}$ ,  $2 \times 10^{15}$ , and  $1 \times 10^{16}$  cm $^{-2}$  for G10, G19, and G29, respectively. Klaassen et al. (2009) have derived a temperature of  $323 \pm 105$  K for G10 using the rotational diagram method. This value is 4 times higher than our estimated temperature. However, these authors have used the optically thick  $\text{CH}_3\text{CN}$  (12–11) lines to derive  $T_{\text{rot}}$ , and thus, their value should be taken as an upper limit. Wu et al. (2009) have estimated a temperature of 552 K for G19 using the rotational diagram method for  $\text{CH}_3\text{CN}$  (18–17). This value is about 2.5 times higher than our estimated temperature. This discrepancy is due to the fact that these authors have used the optically thick  $\text{CH}_3\text{CN}$  lines in their calculations. In fact, Furuya et al. (2010), who have only fitted the optically thin  $\text{CH}_3^{13}\text{CN}$  (18–17) lines in the rotation diagram, have obtained a temperature estimate of 208 K, similar to our value. Finally, Olmi et al. (2003) have estimated a temperature of 150 K for G29 by using the rotational diagram for  $\text{CH}_3^{13}\text{CN}$  (6–5) and vibrationally ex-



**Table 5.** Parameters of the toroids

Core	$T_{\text{rot}}^a$ (K)	$R^b$ (pc)	$M_{\text{gas}}^b$ ( $M_{\odot}$ )	$V_{\text{rot}}$ ( $\text{km s}^{-1}$ )	Vel. gradient ( $\text{km s}^{-1} \text{pc}^{-1}$ )	$\Delta V^c$ ( $\text{km s}^{-1}$ )	$\theta_{\text{CH}_3\text{CN}}^d$ (arcsec)	$M_{\text{vir}}^e$ ( $M_{\odot}$ )	$M_{\text{dyn}}^f$ ( $M_{\odot}$ )	$M_{\text{inf}}^g$ ( $M_{\odot} \text{yr}^{-1}$ )	$t_{\text{inf}}$ (yr)	$t_{\text{ff}}$ (yr)
G10	87	0.016	82	2.1	131	6	3''.0	149	33	$2 \times 10^{-2}$	$4 \times 10^3$	$4 \times 10^3$
G19	244	0.031	415	1.0	32	10	1''.2	615	14	$3 \times 10^{-2}$	$15 \times 10^3$	$5 \times 10^3$
G29	158	0.011	28	1.6	145	9	1''.5	173	13	$8 \times 10^{-3}$	$4 \times 10^3$	$4 \times 10^3$

(a) From the rotational diagram method.

(b) Radius and mass of the toroids estimated from the 1.4 mm continuum emission.

(c) Line width of CH<sub>3</sub>CN (12–11).

(d) Deconvolved average diameter of the 50% contour of the CH<sub>3</sub>CN (12–11) emission.

(e) Virial mass estimated assuming a spherical clump with a density distribution with  $p=1.5$ . The values should be multiplied by 1.25 for  $p=0$ , and by 0.75 for  $p=2$  (see Sect. 5.3).

(f) Computed assuming an inclination angle with respect to the plane of the sky of 45°.

(g) Computed assuming  $V_{\text{inf}} = V_{\text{rot}}$ .

cited CH<sub>3</sub>CN (6–5). This value of  $T_{\text{rot}}$  is consistent with our estimate.

The masses of the HMCs have been estimated from the 1.4 mm dust continuum emission assuming a dust opacity of  $\simeq 0.8 \text{ cm}^2 \text{ g}^{-1}$  at 1.4 mm (Ossenkopf & Henning 1994), a gas-to-dust ratio of 100, and a dust temperature equal to  $T_{\text{rot}}$ . Table 5 gives the radius,  $R$  and masses,  $M_{\text{gas}}$ , of the cores together with  $T_{\text{rot}}$ . We derived a mass of  $82 M_{\odot}$  for G10. Klaassen et al. (2009) have estimated a mass of  $136 M_{\odot}$  at 1.4 mm, assuming a dust opacity of  $\simeq 18.87 \text{ cm}^2 \text{ g}^{-1}$  at 2400 GHz (Hildebrand 1983), a dust-to-gas mass ratio of 100,  $\beta=1.5$ , a temperature of 323 K (P. D. Klaassen 2010, private communication), and a distance of 6 kpc. Using the same parameters, we obtain a mass of  $102 M_{\odot}$  at 1.4 mm.

For G19, the estimated HMC mass is  $415 M_{\odot}$ . The core mass calculated at 900  $\mu\text{m}$  by Wu et al. (2009) is  $15 M_{\odot}$ . These authors have estimated the mass by assuming  $\beta=1.5$ , a temperature of 552 K and a distance of 4 kpc. Note however, that Furuya et al. (2010) have estimated a mass of the HMC of  $1300 M_{\odot}$  ( $1580 M_{\odot}$  taking into account the other two submillimeter sources in the region) at 900  $\mu\text{m}$  for a dust opacity of  $\simeq 0.005 \text{ cm}^2 \text{ g}^{-1}$  at 230 GHz (Preibisch et al. 1993), a dust-to-gas mass ratio of 100,  $\beta=1$ , a temperature of 80 K, and a distance of 12.6 kpc. Using the same dust opacity index, temperature and distance as Wu et al. (2009), the estimated dust mass would be  $16 M_{\odot}$ , whereas the mass would be  $2142 M_{\odot}$  using the same parameters as those of Furuya et al. (2010). On the other hand, Furuya et al. (2005) have estimated a mass of  $800 M_{\odot}$  from the dust emission at 3.3 mm, assuming a Preibisch et al. (1993) dust opacity law,  $\beta=1.5$ , a temperature of 65 K, and a distance of 3.5 kpc. Using the same dust opacity law, temperature, and distance, we would obtain a mass of  $245 M_{\odot}$  from the HMC dust emission at 2.7 mm. These discrepancies among the values give an idea of how uncertain the values of the dust masses are and how important to have an accurate estimate of the distance is.

For G29, we derived a HMC mass of  $28 M_{\odot}$ . Maxia et al. (2001) have estimated a mass of  $2900 M_{\odot}$  at 3.4 mm, assuming a Preibisch et al. (1993) dust opacity law, a dust-to-gas mass ratio of 100,  $\beta=2$ , a temperature of 83 K and a distance of 6 kpc. Using the same opacity law and  $\beta$  coefficient, and distance, Olmi et al. (2003) have estimated a mass of  $320 M_{\odot}$  at 2.7 mm. This could indicate that the thermal dust flux estimated by Maxia et al. (2001) could still have some free-free contribution. Assuming the same

opacity law, temperature and distance, the gas mass estimated from our observations at 1.4 mm would be  $270 M_{\odot}$ .

## 5.2. Physical parameters of the CO outflows

Figure 5 shows the molecular outflows mapped in <sup>13</sup>CO (1–0) and <sup>13</sup>CO (2–1) and towards G19 and G29, respectively. The parameters of the outflows are given in Table 6. Note that the parameters have not been corrected for inclination. The size of the lobes  $R$ , mass  $M$ , outflow mass loss rate  $\dot{M}_{\text{out}}$ , momentum  $P$ , kinetic energy  $E$ , momentum rate in the outflows  $F$ , and dynamical timescale  $t_{\text{out}}$  were derived from the <sup>13</sup>CO emission for the velocities ranges indicated in Fig. 5 and in Table 6. The dynamical timescale of the blueshifted and redshifted lobes has been estimated as  $t_{\text{out}} = R/V_{\text{out}}$ , where  $V_{\text{out}}$  is the difference in absolute value between the maximum blueshifted or redshifted velocity and the systemic velocity (see Table 1). The  $t_{\text{out}}$  of the outflow is the maximum dynamical timescale of the two lobes. The rest of the parameters have been calculated for the blueshifted and redshifted lobes separately, and then added to obtain the total value. The [<sup>13</sup>CO]/[H<sub>2</sub>] abundance ratio was estimated following Wilson and Rood (1994), and assuming an [H<sub>2</sub>]/[CO] abundance ratio of  $10^4$  (e.g. Scoville et al. 1986). We assumed an excitation temperature,  $T_{\text{ex}}$ , of 40 K. The values estimated for the G19 outflow are 1.7 (1.9) times smaller (higher) if  $T_{\text{ex}}$  is 20 K (80 K). On the other hand, the parameters of the G29 outflow are 1.4 (1.7) times smaller (higher) if  $T_{\text{ex}}$  is 20 K (80 K).

As seen in Table 6, the values of  $M$ ,  $P$ , and  $E$  of the G19 outflow are about 30–90 times higher than those of the G29 outflow. The values of  $\dot{M}_{\text{out}}$  and  $F$  are comparable. The dynamical timescale of the G29 outflow is one order of magnitude smaller than that of the G19 outflow. The range of values obtained for G19 and G29, especially the outflow masses, are consistent with those estimated through interferometric observations for other well-studied HMCs (e.g. Furuya et al. 2002, 2008). Regarding the mass loss rates,  $10^{-4}$ – $10^{-3} M_{\odot} \text{ yr}^{-1}$ , the values are consistent with those found for other massive molecular outflows. Finally, the dynamical timescales of the outflows,  $\sim 10^4$  yr, are consistent with the values estimated by Furuya et al. (2002, 2008).

## 5.3. Dense gas kinematics

In the last years, we have detected clear velocity gradients in more than 5 HMCs (Beltrán et al. 2004, 2005; Furuya et

**Table 6.** Properties of the molecular outflows

HMC	Lobe	$V^a$ (km s <sup>-1</sup> )	$R^b$ (pc)	$M^c$ ( $M_\odot$ )	$\dot{M}_{\text{out}}$ ( $M_\odot$ yr <sup>-1</sup> )	$P^d$ ( $M_\odot$ km s <sup>-1</sup> )	$E^d$ (10 <sup>46</sup> erg)	$F_{\text{out}}^d$ ( $M_\odot$ km s <sup>-1</sup> yr <sup>-1</sup> )	$t_{\text{out}}$ (yr)
G19	Blue	[+24.6, +34.8]	0.48	78	$2.8 \times 10^{-3}$	759	7.7	$2.8 \times 10^{-2}$	$3 \times 10^4$
	Red	[+45, +48.4]	0.38	59	$1.1 \times 10^{-3}$	298	1.5	$0.6 \times 10^{-2}$	$5 \times 10^4$
	Total		0.86	137	$2.5 \times 10^{-3}$	1057	9.2	$2.0 \times 10^{-2}$	$5 \times 10^4$
G29	Blue	[-77.9, +88.4]	0.05	0.8	$0.4 \times 10^{-3}$	12	0.2	$0.6 \times 10^{-2}$	$2 \times 10^3$
	Red	[+105.9, +116.4]	0.05	0.7	$0.2 \times 10^{-3}$	8	0.1	$0.3 \times 10^{-2}$	$3 \times 10^3$
	Total		0.10	1.5	$0.5 \times 10^{-3}$	20	0.3	$0.7 \times 10^{-2}$	$3 \times 10^3$

(a) Range of outflow velocities.

(b) Size of the lobe.

(c) Assuming an excitation temperature of 40 K.

(d) Momenta and kinetic energies are calculated relative to the cloud velocity.

al. 2008) that have been interpreted, in most of the cases, as produced by rotating toroids oriented perpendicularly to the bipolar outflow driven by the massive YSO(s) embedded in the HMC. As already done to search for velocity gradients in the HMCs G24.78+0.08 and G31.41+0.31 (Beltrán et al. 2004, 2005), we simultaneously fitted multiple CH<sub>3</sub>CN (12–11)  $K$ -components, assuming identical line widths and fixing their separations to the laboratory values, at each position where CH<sub>3</sub>CN is detected. In this case, we fitted simultaneously the  $K = 0, 1, 2,$  and  $3$  components.

Figure 7 shows the CH<sub>3</sub>CN (12–11) emission averaged under the  $K = 0, 1, 2,$  and  $3$  components overlaid on the CH<sub>3</sub>CN (12–11) line peak velocity obtained with the multiple Gaussian fits. As seen in the LSR velocity maps (Fig. 7), all cores show clear velocity gradients, with  $V_{\text{LSR}}$  increasing steadily along well-defined directions. As we will see in the next sections, the most plausible explanation for the velocity gradients observed in the HMCs is rotation. Therefore, following Beltrán et al. (2004, 2005), we have calculated the parameters of the rotating toroids (see Table 5). The rotation velocity  $V_{\text{rot}}$ , has been estimated as half the velocity range measured in the gradients. The virial mass  $M_{\text{vir}}$  was estimated from CH<sub>3</sub>CN (12–11) assuming a spherical clump with a power-law density distribution  $\rho \propto r^p$ , with  $p=1.5$ , and neglecting contributions from the magnetic field and surface pressure.  $M_{\text{vir}}$  was computed following the expression  $M_{\text{vir}} = 0.407 d \theta_{\text{CH}_3\text{CN}} \Delta V^2$ , where the distance  $d$  is in kpc, the angular diameter,  $\theta_{\text{CH}_3\text{CN}}$ , in arcsec, and the CH<sub>3</sub>CN (12–11) line width,  $\Delta V$ , in km s<sup>-1</sup>. The values given in Table 5 should be multiplied by 1.25 for a homogeneous density distribution,  $p=0$ , and by 0.75 for a density distribution with  $p=2$ . The dynamical mass  $M_{\text{dyn}}$  was computed assuming equilibrium between centrifugal and gravitational forces from the expression  $M_{\text{dyn}} = V_{\text{rot}} R/G \sin^2 i$ , where  $i$  is the inclination angle of the toroid with respect to the plane of the sky, assumed to be 90° for an edge on toroid. Because the inclination angle of the toroids is unknown, we arbitrarily assumed  $i = 45^\circ$ . The mass infall rate has been computed from the expression  $\dot{M}_{\text{inf}} = M_{\text{gas}} 2 V_{\text{inf}}/R$  assuming that the infall velocity  $V_{\text{inf}}$  is equal to the rotation velocity following Allen et al. (2003). We have estimated the lifetimes of the toroids in two different ways, one by measuring the infall timescale  $t_{\text{inf}}$  as  $M_{\text{gas}}/\dot{M}_{\text{inf}}$ , and the other one by estimating the free-fall time  $t_{\text{ff}}$ . The values are given in Table 5. The free-fall time has been estimated from the expression  $t_{\text{ff}} \sim 3.4 \times 10^7 / N_{\text{H}_2}^{1/2}$  yr (Eq. [3.5] of Hartmann 1998), where  $N$ , the number den-

sity of molecular hydrogen gas, is  $3 M_{\text{gas}}/4 \pi R^3 2.8 m_{\text{H}}$ . The parameters of the rotating structures are consistent with those estimated by Beltrán et al. (2004) for the toroids in G24.78+0.08 and G31.41+0.31 (see their Table 1).

### 5.3.1. G10.62–0.38

The CH<sub>3</sub>CN LSR velocity map towards G10 shows a clear velocity gradient with velocity increasing from SE to NW (Fig. 7). This velocity gradient has the same direction as that observed in NH<sub>3</sub> by Sollins & Ho (2005), and more recently in SO<sub>2</sub> by Klaassen et al. (2009), although, the SO<sub>2</sub> gradient is not as clear as the one seen in NH<sub>3</sub> or in CH<sub>3</sub>CN. The fact that the direction of the gradient is almost perpendicular to the direction of the molecular outflow observed towards this HMC (see Fig. 7; Keto & Wood 2006; Klaassen et al. 2009; López-Sepulcre et al. 2009), suggests that it is caused by the rotation of the core.

As seen in Table 5,  $M_{\text{gas}}$  and  $M_{\text{vir}}$  are comparable, suggesting that, in principle, turbulence could support the toroid. On the other hand,  $M_{\text{gas}}$  is 2.5 times larger than  $M_{\text{dyn}}$ , suggesting that the toroid could be unstable. Note, however, that  $M_{\text{dyn}}$  has been calculated for an inclination angle  $i = 45^\circ$  with respect to the plane of the sky. For  $i = 25^\circ$ , the two become equal. The  $\dot{M}_{\text{inf}}$  value is high, of the order of  $10^{-2} M_\odot$  yr<sup>-1</sup>, but comparable to what has been found in other high-mass star-forming regions (Beltrán et al. 2004; Fontani et al. 2002). The  $t_{\text{inf}}$  and  $t_{\text{ff}}$  timescales are consistent and of the order of a few  $10^3$  yr. Unfortunately, we have not been able to estimate the parameters of the outflow (see Sect. 4.3) to compare the timescale of the toroid with that of the outflow, and the infall rate with the mass loss rate.

### 5.3.2. G19.61–0.23

The CH<sub>3</sub>CN LSR velocity map towards G19 shows a clear velocity gradient with velocity increasing in an almost S-N direction (Fig. 7). A similar velocity gradient has been observed in CH<sub>3</sub>CN (18–17) by Furuya et al. (2010). As seen in Fig. 5, the outflow associated with this HMC seems to be oriented approximately E-W. Therefore, as for G10, the most plausible explanation of this gradient is rotation.

As seen in Table 5,  $M_{\text{gas}}$  and  $M_{\text{vir}}$  are comparable, suggesting that, in principle, turbulence, magnetic fields, and/or thermal pressure could support the toroid. On the other hand,  $M_{\text{gas}}$  is 30 times larger than  $M_{\text{dyn}}$ . Even if

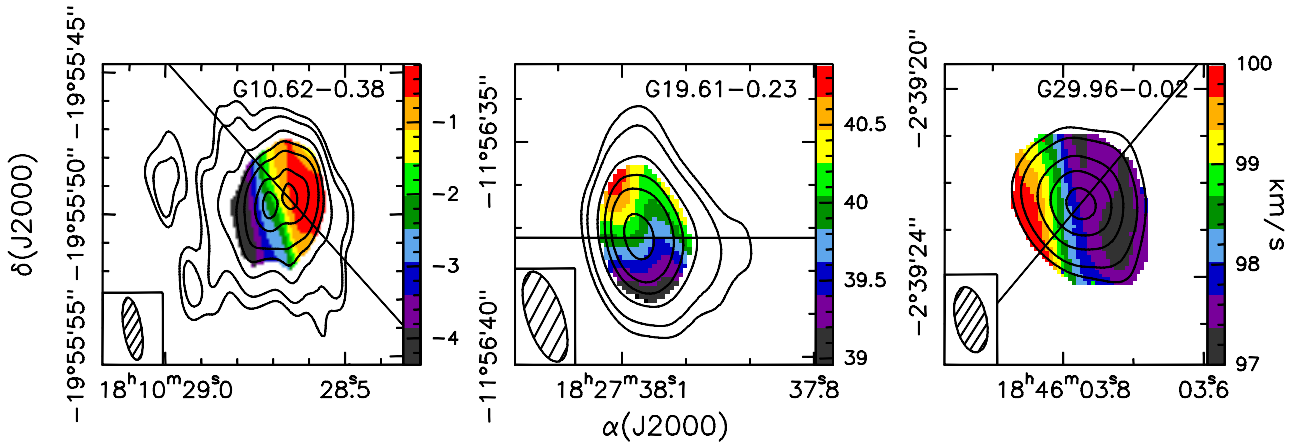


**Fig. 7.** Overlay of the PdBI CH<sub>3</sub>CN (12–11) emission averaged under the  $K = 0, 1, 2,$  and  $3$  components (*contours*) on the CH<sub>3</sub>CN (12–11) line peak velocity obtained with a Gaussian fit (*colors*) towards the cores G10 (*left*), G19 (*middle*), and G29 (*right*). The color levels in km s<sup>-1</sup> are indicated in the wedge to the right of each panel. Contours for CH<sub>3</sub>CN (12–11) are the same as in Fig. 1. The straight line indicates the direction of the molecular outflow (Keto & Wood 2006; this paper). The synthesized beam is shown in the lower left-hand corner.

$i$  were 10°,  $M_{\text{gas}}$  would still be almost 2 times greater. Therefore, this suggests that the G19 toroid is highly unstable and it is probably undergoing collapse. Further support to the collapse of this toroid is provided by <sup>13</sup>CO (2–1). As mentioned in Sect. 4.3, the <sup>13</sup>CO (2–1) transition for G19 is affected by absorption at redshifted velocities (see Fig. 5). A prominent inverse P-Cygni profile has also been observed in <sup>13</sup>CO and C<sup>18</sup>O (3–2), and CN (3–2) with the Submillimeter Array (Wu et al. 2009; Furuya et al. 2010). The <sup>13</sup>CO (3–2) line exhibits absorption from 41.5 to 48 km s<sup>-1</sup>, and the peak of the absorption is at 43.8 km s<sup>-1</sup> (Wu et al. 2009). Such a profile is similar to the one observed by us in <sup>13</sup>CO (2–1), for which the absorption is visible from 41.6 to 54.1 km s<sup>-1</sup>, and the peak is at 45.4 km s<sup>-1</sup>. Figure 8 shows the map of the <sup>13</sup>CO (2–1) absorption averaged over the velocity interval 41.6–54.1 km s<sup>-1</sup> overlaid on the 1.4 mm continuum emission. As seen in this figure, the absorption is well correlated with the continuum emission, and the peak of the absorption coincides with that of the continuum emission.

Similar inverse P-Cygni profiles due to redshifted absorption against the dust continuum emission or an HII region have already been observed towards other massive star-forming regions such as G24.78+0.08 (Beltrán et al. 2006), G31.41+0.31 (Girart et al. 2009; Frau et al., in preparation), and W51 IRS2 (Zapata et al. 2008). In all cases, the redshifted absorption has been interpreted as the signature of infall towards the core center. The same interpretation has been proposed by Wu et al. (2009) and Furuya et al. (2010) for the inverse P-Cygni profiles observed in <sup>13</sup>CO and C<sup>18</sup>O (3–2), and CN (3–2) towards G19. The <sup>13</sup>CO (2–1) line brightness temperature ( $T_{\text{B}} \simeq -10.9$  K) measured along the line-of-sight towards the position of the HMC is comparable to the continuum brightness temperature ( $T_{\text{c}} \simeq 10.3$  K). Hence, we have not been able to estimate the excitation temperature of the absorbing gas.

Taking into account that the systemic velocity  $V_{\text{LSR}}$  of G19 is 41.6 km s<sup>-1</sup> and that the peak of the redshifted absorption is at 45.4 km s<sup>-1</sup>, we have estimated the infall velocity as  $V_{\text{inf}} = |V_{\text{LSR}} - V_{\text{redshifted}}| = 3.8$  km s<sup>-1</sup>, following Beltrán et al. (2006). The  $V_{\text{inf}}$  estimated from <sup>13</sup>CO (3–2) is 3.5 km s<sup>-1</sup> (Wu et al. 2009) and 4 km s<sup>-1</sup> (Furuya et

al. 2010), whereas that from CN (3–2) is 6.0 km s<sup>-1</sup> (Wu et al. 2009). Note that the  $V_{\text{inf}}$  estimated from the redshifted absorption is higher than the infall velocity used to estimate  $\dot{M}_{\text{inf}}$  and  $t_{\text{inf}}$  in Table 5, which is 1 km s<sup>-1</sup>. This value is a rough estimate of the infall velocity, hence the discrepancy between the two  $V_{\text{inf}}$  estimates is not surprising. What this discrepancy indicates is that infall is stronger than rotation. Assuming  $V_{\text{inf}} = 3.8$  km s<sup>-1</sup>,  $\dot{M}_{\text{inf}}$  estimated from  $M_{\text{gas}}$  (see Sect. 5.3) is 0.1  $M_{\odot}$  yr<sup>-1</sup>, and  $t_{\text{inf}} = 4 \times 10^3$  yr. This latter value is more similar to the estimated  $t_{\text{ff}}$ .

Following Beuther et al. (2002), one can estimate the mass accretion rate  $\dot{M}_{\text{acc}}$  from the outflow mass loss rate  $\dot{M}_{\text{out}}$ . According to these authors, the mass loss rate of the outflow is related to the mass loss rate of the internal jet entraining the outflow  $\dot{M}_{\text{jet}}$  as  $\dot{M}_{\text{out}} = \dot{M}_{\text{jet}} V_{\text{jet}}/V_{\text{out}}$ , where the ratio between the jet velocity  $V_{\text{jet}}$  and the molecular outflow velocity  $V_{\text{out}}$  is  $\sim 20$ . Assuming a ratio between  $\dot{M}_{\text{jet}}$  and the mass accretion rate onto the protostar  $\dot{M}_{\text{acc}}$  of approximately 0.3 (Tomisaka 1998; Shu et al. 1999), one finds that  $\dot{M}_{\text{out}} = 20 \dot{M}_{\text{jet}} = 6 \dot{M}_{\text{acc}}$ . Therefore, for G19,  $\dot{M}_{\text{acc}}$  would be  $\sim 4 \times 10^{-4} M_{\odot}$  yr<sup>-1</sup>.  $\dot{M}_{\text{acc}}$  is about two orders of magnitude smaller than  $\dot{M}_{\text{inf}}$  (see Table 5). Note that the outflow parameters have not been corrected for inclination.  $\dot{M}_{\text{out}}$  is to be multiplied by  $\tan i$  to correct for the inclination angle  $i$  of the flow with respect to the line-of-sight. However, a correction by a factor  $> 10$  would imply  $i > 84^\circ$ , which seems very unlikely because rotation would be very difficult to detect in such a face-on structure. Therefore, the outflow inclination cannot account for the difference between  $\dot{M}_{\text{acc}}$  and  $\dot{M}_{\text{inf}}$ . In addition, part of the extended outflow emission could have been filtered out by the interferometer, and therefore  $\dot{M}_{\text{out}}$  and  $\dot{M}_{\text{acc}}$  should be considered as lower limits. However, after inspecting the <sup>13</sup>CO channel maps, we conclude that the missing flux problem is unlikely to account for 2 orders of magnitude of difference in the estimates of the outflow parameters. Moreover, the single-dish study of López-Sepulcre et al. (2010) have obtained a similar result with mass accretion rates 2 to 4 orders of magnitude smaller than the infall rates for a sample of high-mass cluster forming clumps. Their inter-

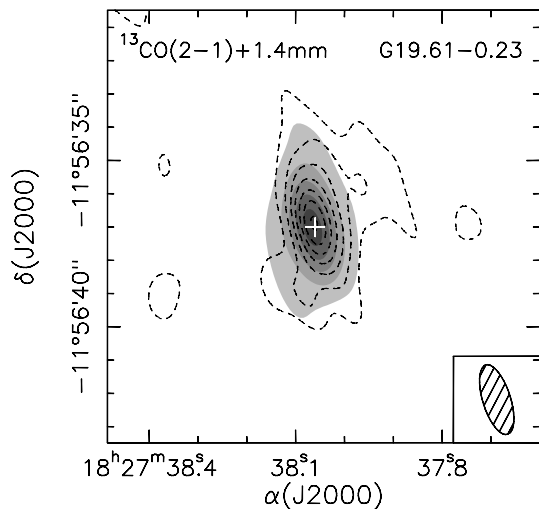


**Fig. 8.** Overlay of the  $^{13}\text{CO}$  (2–1) averaged absorption (*dashed contours*) on the 1.4 mm continuum emission (*greyscale*). The absorption has been averaged over the velocity interval  $41.6\text{--}54.1\text{ km s}^{-1}$ . Negative contours range from  $-0.1$  to  $-0.7\text{ Jy beam}^{-1}$  in steps of  $-0.1\text{ Jy beam}^{-1}$  ( $1\sigma \simeq 0.03\text{ Jy beam}^{-1}$ ). Greyscale contours for the continuum emission are the same as in Fig. 1. The white cross marks the position of the 1.4 mm continuum emission peak. The synthesized beam is shown in the lower right-hand corner.

pretation is that  $\dot{M}_{\text{inf}}$  represents the infall of the material onto a cluster of stars, while  $\dot{M}_{\text{acc}}$  corresponds to the material being accreted onto a single massive star, responsible for the massive molecular outflow detected. The large masses and luminosities involved suggest that these rotating toroids likely host a stellar cluster rather than a single star (Beltrán et al. 2005; Cesaroni et al. 2006).

### 5.3.3. G29.96–0.02

The  $\text{CH}_3\text{CN}$  LSR velocity map towards G29 shows a clear velocity gradient with velocity increasing in from W to E (Fig. 7). Cesaroni et al. (1998) and Olmi et al. (2003) have detected in  $\text{NH}_3$  and  $\text{CH}_3\text{CN}$  a velocity gradient across the HMC approximately along the same direction by fitting the peak of the emission at each spectral channel. This is similar to the velocity gradient observed in  $\text{HN}^{13}\text{C}$  by Beuther et al. (2007b). As seen in Fig. 5, the embedded YSO(s) in this HMC powers a molecular outflow with a SE–NW direction. This outflow has also been mapped in  $\text{H}_2\text{S}$  (Gibb et al. 2004) and  $\text{SiO}$  (8–7) (Beuther et al. 2007b). The velocity gradient is clearly not perpendicular to the molecular outflow. Note that also for G10 and G19 the velocity gradients are not exactly perpendicular to the molecular outflows (see Fig. 7). Although for these HMCs the discrepancy is of a few degrees. One possible explanation for the non-perpendicularity of the velocity gradient could be the highly elliptical beam of the PdBI observations. According to Guilloteau & Dutrey (1998), to analyze the velocity field, it is essential to use a circular beam, otherwise, velocity gradients in marginally resolved objects may be severely distorted. To investigate this effect, we re-analyze the OVRO  $\text{CH}_3\text{CN}$  (6–5) observations towards G29 carried out by Olmi et al. (2003), with the simultaneous fit of the  $\text{CH}_3\text{CN}$

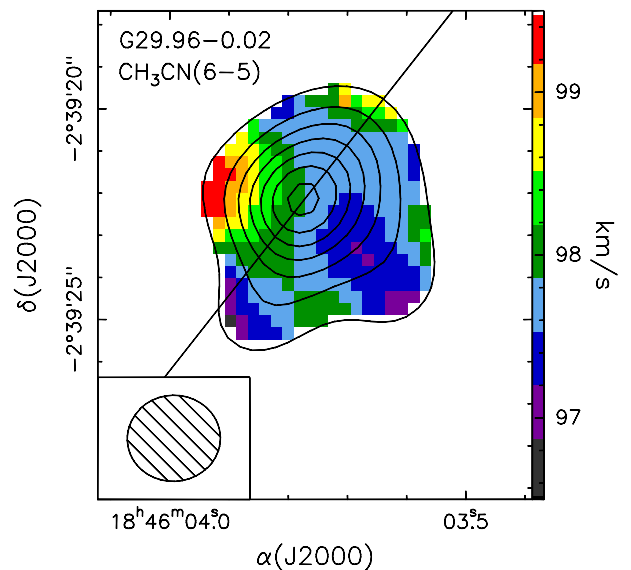


**Fig. 9.** Overlay of the OVRO  $\text{CH}_3\text{CN}$  (6–5) emission from Olmi et al. (2003) averaged under the  $K = 0$  and 1 components (*contours*) on the  $\text{CH}_3\text{CN}$  (6–5) line peak velocity obtained with a Gaussian fit (*colors*) towards the core G29. The color levels in kilometers per second are indicated in the wedge to the right. Contours for  $\text{CH}_3\text{CN}$  (6–5) are range from  $0.1$  to  $0.7\text{ Jy beam}^{-1}$  in steps of  $0.1\text{ Jy beam}^{-1}$  ( $1\sigma \simeq 0.03\text{ Jy beam}^{-1}$ ). The straight line indicates the direction of the molecular outflow. The synthesized beam is shown in the lower left-hand corner.

$K$ -components. Figure 9 shows the  $\text{CH}_3\text{CN}$  (6–5) emission averaged under the  $K = 0$  and 1 components overlaid on the  $\text{CH}_3\text{CN}$  (6–5) line peak velocity. As seen in this plot, the synthesized beam of these observations is almost circular, and the velocity gradient shows a SW–NE direction. This direction is perpendicular to that of the molecular outflow, and therefore, we interpret the velocity gradient as due to rotation.

As seen in Table 5,  $M_{\text{vir}}$  is 6 times higher than  $M_{\text{gas}}$ , suggesting that, in principle, turbulence, magnetic fields, and/or thermal pressure could support the toroid. On the other hand,  $M_{\text{gas}}$  is 2 times larger than  $M_{\text{dyn}}$ . For  $i \sim 30^\circ$ , the two become comparable. The difference between  $M_{\text{gas}}$  and  $M_{\text{dyn}}$  could suggest that the G29 toroid is unstable and probably undergoing collapse. As mentioned in Sect. 4.3, the  $^{13}\text{CO}$  (2–1) transition towards the G29 HMC is affected by absorption at redshifted velocities (see Fig. 5). In this case, the absorption is less clear than for G19. Probably this is because emission and absorption are mixed along the line-of-sight towards the HMC, making the latter less evident. The peak of the absorption is at  $\sim 104\text{ km s}^{-1}$ , therefore  $V_{\text{inf}}$  is  $\sim 5\text{ km s}^{-1}$ . Note that the  $V_{\text{inf}}$  estimated from the redshifted absorption is higher than the infall velocity used to estimate  $\dot{M}_{\text{inf}}$  and  $t_{\text{inf}}$  in Table 5, which is  $1.6\text{ km s}^{-1}$ . Assuming  $V_{\text{inf}} = 5\text{ km s}^{-1}$ ,  $\dot{M}_{\text{inf}}$  estimated from  $M_{\text{gas}}$  (see Sect. 5.3) is  $0.03 M_\odot\text{ yr}^{-1}$ , and  $t_{\text{inf}} = 1 \times 10^3\text{ yr}$ . As already seen for the other toroids,  $\dot{M}_{\text{inf}}$  is high, of the order of  $10^{-2} M_\odot\text{ yr}^{-1}$ , but comparable to what has been found in other high-mass star-forming regions. The  $t_{\text{inf}}$  and  $t_{\text{ff}}$  timescales are consistent and of the order of  $\sim 10^3\text{ yr}$ .

The mass accretion rate  $\dot{M}_{\text{acc}}$  estimated from the outflow mass loss rate  $\dot{M}_{\text{out}}$  (see previous section) is

$\sim 8 \times 10^{-5} M_{\odot} \text{ yr}^{-1}$ . As for G19 (see previous section), the accretion rate is two orders of magnitude smaller than the infall rate (see Table 5), and neither the inclination of the outflow nor the filtering out of the emission seem able to account for such a discrepancy. Therefore, also in this case, the most plausible explanation for  $\dot{M}_{\text{inf}} \gg \dot{M}_{\text{acc}}$  is that the material of the toroid is infalling onto a cluster of stars instead of a single star, responsible for the molecular outflow.

#### 5.3.4. Absorption towards the G29.96–0.02 UC HII region

Maxia et al. (2001) detected redshifted absorption in the integrated spectra of  $\text{HCO}^+$  (1–0) towards G29. The map of the  $\text{HCO}^+$  (1–0) line averaged over the absorption velocity range, 99–102  $\text{km s}^{-1}$ , shows that the absorption is positionally coincident with the UC HII region (see Fig. 8 of Maxia et al. 2001). To check whether this absorption is also visible in the  $^{13}\text{CO}$  (2–1) line, we have obtained the spectrum towards the peak of the 1.4 mm continuum emission of the UC HII region, and, following Maxia et al. (2001), over the  $3\sigma$  contour level of the 1.4 mm continuum emission towards G29; that is, a region including the HMC and the UC HII region (Fig. 10). As seen in the top panel of this figure, deep and broad absorption is clearly visible towards the UC HII region. When integrating the  $^{13}\text{CO}$  (2–1) emission over the  $3\sigma$  contour level of the 1.4 mm continuum emission, the emission combines with the absorption, making it less pronounced. However, the absorption is still clearly visible at a velocity of  $\sim 104 \text{ km s}^{-1}$ . This velocity is different from that of the  $\text{HCO}^+$  absorption, which according to Maxia et al. (2001) is  $98.8 \text{ km s}^{-1}$ . This may mean that this  $^{13}\text{CO}$  absorption feature is not real but due to the interferometer resolving out extended emission at this velocity. Alternatively, the  $^{13}\text{CO}$  emission could be stronger and more extended than the  $\text{HCO}^+$  emission, and thus, the combination of emission and absorption could produce an absorption feature at a velocity interval different from that observed in  $\text{HCO}^+$ . From Fig. 10 and the  $^{13}\text{CO}$  (2–1) channel maps, one sees that the redshifted absorption is visible towards the position of the UC HII region in the velocity range 98.9–105.9  $\text{km s}^{-1}$ . The  $^{13}\text{CO}$  (2–1) map averaged over this velocity interval is shown in Fig. 11. This map is similar to the  $\text{HCO}^+$  integrated map of Maxia et al. (2001), and clearly shows absorption towards the UC HII region, whereas emission is visible towards the HMC and the NE. For these reasons, we believe that the  $^{13}\text{CO}$  absorption feature at  $\sim 104 \text{ km s}^{-1}$  is real, although only complementary single-dish data may prove this.

The  $^{13}\text{CO}$  (2–1) line brightness temperature  $T_{\text{B}}$  measured along the line-of-sight towards the position of the UC HII region is  $-4.5 \text{ K}$ . Within the uncertainties, this is comparable to the continuum brightness temperature  $T_{\text{c}} \simeq 3.4 \text{ K}$ , which shows that the continuum photons are almost totally absorbed by the  $^{13}\text{CO}$  gas.

## 6. Rotating toroids in massive star forming regions

In recent years a number of massive, rotating structures have been discovered in high-mass YSOs (see Table 7). Following Cesaroni et al. (2006), these rotating structures should be classified into two classes on the basis of the ratio between the mass of the rotating structure and that of the star. On the one hand, rotating structures with masses

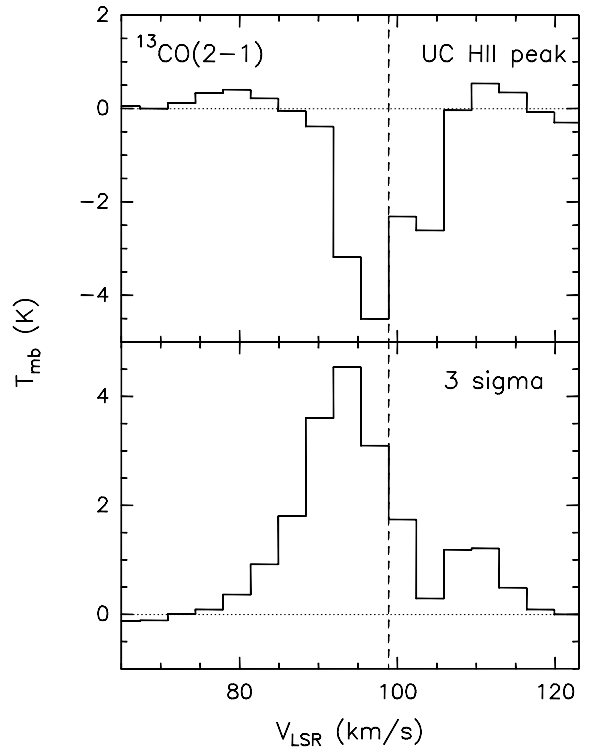


**Fig. 10.**  $^{13}\text{CO}$  (2–1) integrated spectra towards the peak of the 1.4 mm continuum emission of the UC HII region (*top*), and over the  $3\sigma$  contour level of the 1.4 mm continuum emission (*bottom*) towards G29. The dashed vertical line indicates the systemic velocity of each core.

lower than the mass of the central, star, typically found around B-type stars, are centrally supported disks. On the other hand, structures having masses in excess of several  $10 M_{\odot}$ , much greater than the mass of the central star(s), and found around O-type stars, should be called toroids.

In Beltrán et al. (2004, 2005) and this work, we have concentrated on the study of the large rotating toroids around O-type stars, deriving their properties and comparing them to disks around low-mass YSOs. The sizes of the toroids are of several 1000 AU, which are an order of magnitude higher than those of accretion disks in solar-type pre-main sequence stars ( $\sim$  a few 100 AU). As already discussed, their masses are much higher than the mass of any central (proto)star. In fact, these toroids are so huge that they may host not just a single star, but a whole cluster. This is completely different from the low-mass scenario, where the disks have masses of a few  $10^{-3}$  to  $10^{-1} M_{\odot}$  (Natta 2000), i.e. 10–100 times smaller than the mass of the central star.

For some of the HMCs hosting rotating toroids, inverse P-Cygni profiles (or redshifted absorption), have also been detected (this work; Sollins et al. 2005; Beltrán et al. 2006; Zapata et al. 2008; Girart et al. 2009; Wu et al. 2009; Furuya et al. (2010)), indicating that these toroids are not only rotating but also infalling. However, one sees that the infall rates are of the order of  $10^{-3}$ – $10^{-2} M_{\odot} \text{ yr}^{-1}$ , while those derived for accretion disks in low-mass YSOs range from  $10^{-9}$  to  $10^{-6} M_{\odot} \text{ yr}^{-1}$  (Hartmann 1998).

Based on this and on the fact that the infall rates are 2 orders of magnitudes greater than the mass accretion rates estimated from the mass loss rates of the correspond-

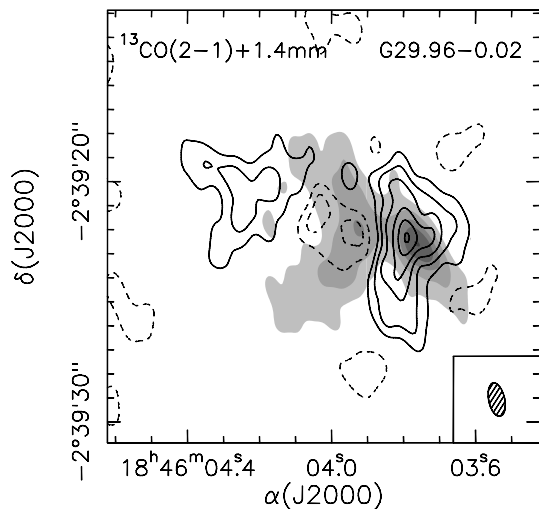


**Fig. 11.** Overlay of the  $^{13}\text{CO}$  (2–1) mean absorption (*dashed contours*) on the 1.4 mm continuum emission (*greyscale*). The absorption has been averaged over the velocity interval 98.9–105.9 km s $^{-1}$ . Negative contours are  $-0.06$  and  $-0.12$  Jy beam $^{-1}$ , while positive contours range from 0.08 to 0.56 in steps of 0.08 Jy beam $^{-1}$  ( $1\sigma \simeq 0.02$  Jy beam $^{-1}$ ). Greyscale contours for the continuum emission are the same as in Fig. 1. The synthesized beam is shown in the lower right-hand corner.

ing outflows (Sects. 5.3.2 and 5.3.3), we propose an scenario in which massive toroids would be transient structures infalling towards a central cluster of forming stars. In this scenario, the circumcluster toroids would be fed by a larger scale reservoir of material, consisting of the parsec-scale clumps surrounding them. The material of the toroids would infall onto the circumstellar disks in the cluster, and then from the disks it would accrete onto the corresponding central stars. In this sense, the circumcluster toroids would be the high-mass analogs of the circumstellar infalling envelopes surrounding low-mass stars, and the embedded circumstellar disks (not imaged yet towards O-type stars; Cesaroni et al. 2006, 2007) would correspond to the accretion disks observed towards Class 0 and I low-mass YSOs.

The differences in the velocity field observed towards low- and high-mass YSOs also support this idea that toroids are qualitatively different from disks. For low-mass stars, the disks undergo Keplerian rotation, while for toroids, Keplerian rotation is not possible on scales of  $10^4$  AU due to the fact that the gravitational potential of the system is dominated by the massive toroid, not by the star. For this reason, it has been proposed that these toroids never reach equilibrium (Cesaroni et al. 2006). They could be transient entities, with timescales of the order of the free-fall time,  $\sim 10^4$  yr. In contrast, according to Natta (2000), low-mass pre-main-sequence disks may live as long as  $10^7$  yr. To study the stability of these structures, we have plotted in Fig. 12 the  $t_{\text{ff}}/t_{\text{rot}}$  ratio versus  $M_{\text{gas}}$ , where the free-fall time  $t_{\text{ff}}$  is proportional to the dynamical timescale needed to refresh the material of the toroid and  $t_{\text{rot}}$  is the rotational period at the outer radius,  $2\pi R/V_{\text{rot}}$ , for a number of disks and toroids around high-mass (proto)stars. The gas masses found in the literature have been estimated assuming different dust opacity laws and, as seen in Sect. 5.1, this is

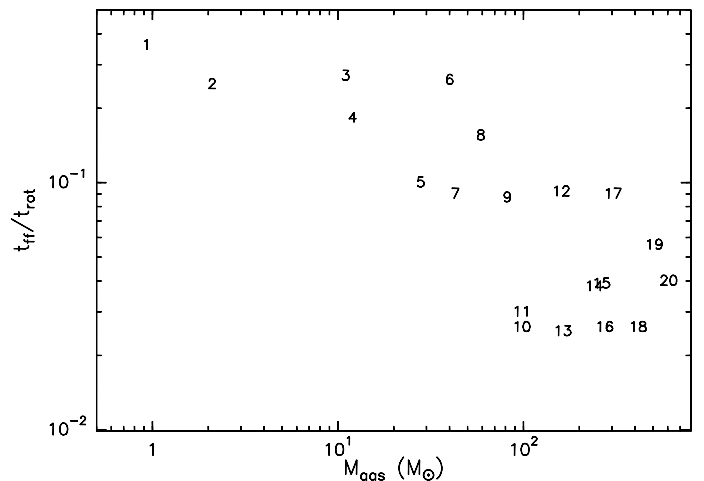


**Fig. 12.** Free-fall timescale to rotational period ratio versus gas mass of known rotating disks or toroids. The masses have been estimated assuming the dust opacities of Ossenkopf & Henning (1994). The numbers correspond to the entries of Table 7.

an important source of uncertainty in the mass determination. Therefore, for all but one case (GH2O 92.67+3.07)<sup>2</sup>, we have re-calculated the gas masses from the dust continuum emission using the dust opacities of Ossenkopf & Henning (1994), with a dust opacity of  $\simeq 0.8$  cm $^2$  g $^{-1}$  at 1.4 mm, i.e. the same used for our sources. We give this in col. 3 of Table 7, while in col. 4 we give the mass estimates found in the literature. Note that for those wavelengths for which the opacity has not been tabulated by Ossenkopf & Henning (1994), we have extrapolated the value from  $\lambda=1.4$  mm assuming  $\beta=2$ . These gas masses have been used to estimate  $t_{\text{ff}}$ , which together with  $t_{\text{rot}}$ , have been calculated following Sect. 5.3 and using the parameters reported in Table 7. Assuming an uncertainty of  $\sim 20\%$  in  $M_{\text{gas}}$ ,  $V_{\text{rot}}$ , and  $R$ , the uncertainty in  $t_{\text{ff}}/t_{\text{rot}}$  would be  $\sim 25\%$ . In all cases, if the structure rotates fast, the infalling material has enough time to settle into a centrifugally supported disk. Vice versa, if the structure rotates slowly, the infalling material does not have enough time to reach centrifugal equilibrium and the rotating structure is a transient toroid. Therefore, the higher the  $t_{\text{ff}}/t_{\text{rot}}$  ratio, the more similar should be the rotating structure to a circumstellar disk. In fact, in Fig. 12, one sees that the less massive structures, which have masses comparable to or lower than that of the central star have the higher  $t_{\text{ff}}/t_{\text{rot}}$  ratio, while the massive toroids have a lower ratio. A typical example of a circumstellar disk in Keplerian rotation around a B-type star is that found towards IRAS 20126+4104 (Cesaroni et al. 2005), while a typical example of rotating toroid around an O-type star is G31.41+0.31 (Beltrán et al. 2004, 2005).

In summary, our findings suggest that massive stars could form by infall/accretion through rotating toroids/disks, although the sizes, masses, timescales, infall, and accretion rates involved are much greater than those of low-mass accretion disks. It is important to stress that although rotation, infall, and outflow have been detected towards massive YSOs, so far no real accretion disk in O-type stars has been imaged yet. However, as already discussed by

<sup>2</sup> The mass of this core has been estimated from CS emission (Bernard et al. 1999).



Cesaroni et al. (2006), real accretion disks might be embedded inside the rotating toroids, and impossible to disentangle from the massive toroids with current instrumentation. Only the new capabilities of the Atacama Large Millimeter Array (ALMA), in terms of sensitivity and resolution, will shed some light on this important issue.

## 7. Conclusions

We have analyzed millimeter high-angular resolution data, obtained with the IRAM PdBI interferometer, of the dust and gas emission towards the HMCs G10.62–0.38, G19.61–0.23, and G29.96–0.02. The aims were to study the structure of the cores, map the molecular outflows powered by the YSOs embedded in the HMCs, and reveal possible velocity gradients indicative of rotation.

The continuum emission at 2.7 mm is clearly dominated by free-free emission from the UC HII region(s), while at 1.4 mm dust emission from the HMCs prevails.

The CH<sub>3</sub>CN (12–11) LSR velocity maps reveal the existence of clear velocity gradients in the three HMCs oriented perpendicular to the direction of the corresponding bipolar outflows. The gradients are interpreted as rotation. The gas temperatures, used to derive the mass of the cores, have been obtained by means of the rotational diagram method, and are in the range of 87–244 K. The diameters and masses of the toroids lie in the range of 4550–12600 AU, and 28–415  $M_{\odot}$ , respectively.

The masses of the cores are comparable to the corresponding virial masses suggesting that turbulence could support the toroids. Given that the dynamical mass is considerably smaller than the mass of the cores, we suggest that the toroids are not centrifugally supported and are possibly undergoing collapse. For G19 and G29, this is also suggested by the redshifted absorption seen in <sup>13</sup>CO (2–1). We infer that infall onto the embedded (proto)stars proceeds with rates of  $\sim 10^{-2} M_{\odot} \text{ yr}^{-1}$ , and on timescales of the order of  $\sim 4 \times 10^3$ – $10^4$  yr. The infall rates derived for G19 and G29 are two orders of magnitude greater than the accretion rates indirectly estimated from the mass loss rate of the corresponding outflows. This suggests that the material in the toroids is not infalling onto a single massive star, responsible for the corresponding molecular outflow, but onto a cluster of stars.

The masses, sizes, and infall rates of the rotating toroids are orders of magnitude higher than those of real accretion disks around lower mass stars, while their lifetimes are much shorter. Also, we find that the higher the mass of the rotating structure, the lower the  $t_{\text{ff}}/t_{\text{rot}}$  ratio is. Therefore, circumstellar disks around B-type stars are centrifugally supported and undergo Keplerian rotation, while massive toroids around O-type stars appear to be transient structures undergoing collapse.

*Acknowledgements.* We thank the staff of IRAM for their help during the observations and data reduction.

## References

- Allen, A., Li, Z.-Y., & Shu, F. H. 2003, *ApJ*, 599, 363  
 Arce, H. G., Santiago-García, J., Jørgensen, J. K. et al. 2008, *A&A*, 481, L21  
 Argon, A. L., Reid, M. J., & Menten, K. M. 2000, *ApJS*, 129, 159  
 Beltrán, M. T., Cesaroni, R., Codella, C. et al. 2006, *Nature*, 443, 427  
 Beltrán, M. T., Cesaroni, R., Neri, R. et al. 2004, *ApJ*, 601, L187  
 Beltrán, M. T., Cesaroni, R., Neri, R. et al. 2005, *A&A*, 435, 901  
 Bernard, J. P., Dobashi, K., & Momose, M. 1999, *A&A*, 350, 197  
 Beuther, H., Churchwell, E. B., McKee, C. F., & Tan, J. C. 2007a, in *Protostars & Planets V*, eds. B. Reipurth, D. Jewitt, & K. Keil (University of Arizona Press), 165  
 Beuther, H., Schilke, P., Sridharan, T. K. et al. 2002, *A&A*, 383, 892  
 Beuther, H., Walsh, A. J., Thorwirth, S. et al. 2008, *A&A*, 481, 169  
 Beuther, H., Zhang, Q., Bergin, E. A. et al. 2007b, *A&A*, 468, 1045  
 Beuther, H., Zhang, Q., Hunter, T. R. et al. 2007c, *A&A*, 473, 493  
 Beuther, H., Zhang, Q., Sridharan, T. K., Chen, Y. 2005, *ApJ*, 628, 800  
 Bonnell, I. A., Larson, R. B., & Zinnecker, H. 2007, in *Protostars & Planets V*, eds. B. Reipurth, D. Jewitt, & K. Keil (University of Arizona Press), 149  
 Bonnell, I. A., Vine, S. G., & Bate, M. R. 2004, *MNRAS*, 349, 735  
 Blum, R. D., Damineli, A., & Conti, P. S. 2001, *AJ*, 121, 3149  
 Cesaroni, R., Churchwell, E., Hofner, P. et al. 1994, *A&A*, 288, 903  
 Cesaroni, R., Felli, M., Jenness, T. et al. 1999, *A&A*, 345, 949  
 Cesaroni, R., Galli, D., Lodato, G. et al. 2006, *Nature*, 444, 703  
 Cesaroni, R., Galli, D., Lodato, G. et al. 2007, in *Protostars & Planets V*, eds. B. Reipurth, D. Jewitt, & K. Keil (University of Arizona Press), 197  
 Cesaroni, R., Hofner, P., Walmsley, C. M., & Churchwell, E. 1998, *A&A*, 331, 709  
 Cesaroni, R., Neri, R., Olmi, L. et al. 2005, *A&A*, 434, 1039  
 Codella, C., Benedettini, M., Beltrán, M. T. et al. 2009, *A&A*, 507, L25  
 De Buizer, J. M., Watson, A. M., Radomski, J. T., Piña, R. K., & Telesco, C. M. 2002, *ApJ*, 564, L101  
 Fontani, F., Cesaroni, R., Caselli, P., & Olmi, L. 2002, *A&A*, 389, 603  
 Forster, J. R., & Caswell, J. L. 1989, *A&A*, 213, 339  
 Furuya, R. S., Cesaroni, R., Codella, C. et al. 2002, *A&A*, 390, L1  
 Furuya, R. S., Cesaroni, R., & Shinnaga, H. 2010, *A&A*, submitted  
 Furuya, R. S., Cesaroni, R., Takahashi, S. et al. 2005, *ApJ*, 624, 827  
 Furuya, R. S., Cesaroni, R., Takahashi, S. et al. 2008, *ApJ*, 673, 363  
 Galván-Madrid, R., Keto, E., Zhang, Q. et al. 2009, *ApJ*, 706, 1036  
 Garay, G., Moran, J. M., Rodríguez, L. F., & Reid, M. J. 1998, *ApJ*, 492, 635  
 Garay, G., Reid, M. J., & Moran, J. M. 1985, *ApJ*, 289, 681  
 Gibb, A. G., Wyrowski, F., & Mundy, L. G. 2004, *ApJ*, 616, 301  
 Girart, J. M., Beltrán, M. T., Zhang, Q. et al. 2009, *Science*, 324, 1408  
 Guilloteau, S., & Dutrey, D. 1998, *A&A*, 339, 467  
 Hartmann, L. 1998 in *Accretion Processes in Star Formation*, Cambridge Astrophysics Series, Vol. 32  
 Hildebrand, R. H. 1983, *QJRAS*, 24, 267  
 Ho, P. T. P., & Haschick, A. D. 1986, *ApJ*, 304, 501  
 Hoffman, I. M., Goss, W. M., Palmer, P., & Richards, A. M. S. 2003, *ApJ*, 598, 1061  
 Hofner, P., & Churchwell, E. 1996, *A&AS*, 120, 283  
 Hunter, T. R., Brogan, C. L., Megeath, S. T., et al. 2006, *ApJ*, 649, 888  
 Keto, E. 2002, *ApJ*, 568, 754  
 Keto, E. R., Ho, P. T. P., & Haschick, A. D. 1988, *ApJ*, 324, 920  
 Keto, E. R., Ho, P. T. P., & Reid, M. J. 1987, *ApJ*, 323, L117  
 Keto, E., & Wood, K. 2006, *ApJ*, 637, 850  
 Klaassen, P. D., Wilson, C. D., Keto, E. R., & Zhang, Q. 2009, *ApJ*, 703, 1308  
 Kolpak, M. A., Jackson, J. M., Bania, T. M. et al. 2003, *ApJ*, 582, 756  
 Krumholz, M. R., Klein, R. I., McKee, C. F., Offner, S. S. R., & Cunningham, A. J. 2009, *Science*, 323, 754  
 Kuiper, R., Klahr, H., Beuther, H., & Henning, T. 2010, *ApJ*, 722, 1556  
 López-Sepulcre, A., Codella, C., Cesaroni, R. et al. 2009, *A&A*, 499, 811  
 López-Sepulcre, A., Cesaroni, R., & Walmsley, C. M. 2010, *A&A*, in press  
 Maxia, C., Testi, L., Cesaroni, R., & Walmsley, C. M. 2001, *A&A*, 371, 287  
 McKee, C. F., & Tan, J. C. 2002, *Nature*, 416, 59  
 McKee, C. F., & Tan, J. C. 2003, *ApJ*, 585, 850  
 Natta, A. 2000 in *Infrared space astronomy, today and tomorrow*. Eds. F. Casoli, J. Lequeux, & F. David, Les Houches Summer School, 70, 193  
 Olmi, L., Cesaroni, R., Hofner, P. et al. 2003, *A&A*, 407, 225  
 Ossenkopf, V., & Henning, Th. 1994, *A&A*, 291, 943  
 Patel, N., Curiel, S., Sridharan, T. K. et al. 2005, *Nature*, 437, 109  
 Plume, R., Jaffe, D. T., & Evans, N. J. II 1992, *ApJS*, 78, 505

**Table 7.** List of rotating disks and toroids in high-mass (proto)stars

Number <sup>a</sup>	Core	$M_{\text{gas}}^{\text{OH}94\text{ }b}$ ( $M_{\odot}$ )	$M_{\text{gas}}^c$ ( $M_{\odot}$ )	$R$ (pc)	$V_{\text{rot}}$ ( $\text{km s}^{-1}$ )	Refs. <sup>d</sup>	$t_{\text{ff}}/t_{\text{rot}}^e$
1	IRAS 20126+4104	0.93	4	0.008	1.3	1,2	0.36
2	Cepheus A HW2	2.1	8 <sup>f</sup>	0.0016	3.0	3	0.25
3	IRAS 23151+5912	11	26	0.010	3.0	4	0.27
4	GH2O 92.67+3.07	12 <sup>g</sup>	12	0.035	1.2	5	0.18
5	G29.96−0.02	28	28	0.011	1.6	6	0.10
6	G20.08−0.14N	40	95 <sup>h</sup>	0.024	3.5 <sup>i</sup>	7	0.26
7	NGC 6334I	43	17	0.0014	5.1	8, 9	0.09
8	IRAS 18089−1732	59	45 <sup>j</sup>	0.010	4.0	10	0.16
9	G10.62−0.38	82	82	0.016	2.1	6	0.09
10	G28.87+0.07	98	100	0.029	0.5	11	0.03
11	G24.78+0.08 C	98	250	0.040	0.5	12	0.03
12	W51 North	160	90	0.068	1.5	13	0.09
13	G24.78+0.08 A2	163	80	0.020	0.75	12	0.03
14	W51e2	241	140	0.010	2.0	14, 15	0.04
15	G24.78+0.08 A1	264	130	0.020	1.5	12	0.04
16	G23.01−0.41	274	380	0.060 <sup>k</sup>	0.6	11	0.03
17	IRAS 18566+0408	304	70	0.034	3.0	16	0.09
18	G19.61−0.23	415	415	0.031	1.0	6	0.03
19	G31.41+0.31	508	490	0.040	2.1	12	0.06
20	NGC 7538S	607	100	0.070	1.35	17	0.04

<sup>a</sup> Number in Fig. 12.<sup>b</sup> Masses estimated assuming the dust opacities of Ossenkopf & Henning (1994; see Sect. 6).<sup>c</sup> Masses from the literature (see Sect. 6).<sup>d</sup> References for the core parameters: 1: Cesaroni et al. (2007); 2: Cesaroni et al. (2005) 3: Patel et al. (2005); 4: Beuther et al. (2007c); 5: Bernard et al. (1999); 6: This work; 7: Galván-Madrid et al. (2009); 8: Hunter et al. (2006); 9: Beuther et al. (2008); 10: Beuther et al. (2005); 11: Furuya et al. (2008); 12: Beltrán et al. (2004); 13: Zapata et al. (2008); 14: Zhang & Ho (1997); 15: Shi et al. (2010); 16: Zhang et al. (2007); 17: Sandell et al. (2003)<sup>e</sup> The free-fall times  $t_{\text{ff}}$  have been estimated from the masses obtained assuming the dust opacities of Ossenkopf & Henning (1994). The uncertainty in  $t_{\text{ff}}/t_{\text{rot}}$  is  $\sim 25\%$ .<sup>f</sup> Mass estimated using  $\beta=2$  (Patel et al. 2005).<sup>g</sup> The mass of this core has been estimated from CS (Bernard et al. 1999) and is the value used to derive  $t_{\text{ff}}$ .<sup>h</sup> Mass estimated using  $\beta=1.5$  (Galván-Madrid et al. 2009).<sup>i</sup>  $V_{\text{rot}}$  is  $\sim 3\text{--}4 \text{ km s}^{-1}$  (Galván-Madrid et al. 2009).<sup>j</sup> Mass estimated assuming a hot core temperature of 100 K (Beuther et al. 2005).<sup>k</sup>  $R$  ranges from 0.055 to 0.068 pc depending on the observational wavelength (Furuya et al. 2008).

- Pratap, P., Megeath, S. T., & Bergin, E. A. 1999, *ApJ*, 517, 799  
 Preibisch, Th., Ossenkopf, V., Yorke, H. W., & Henning, Th. 1993, *A&A*, 279, 577  
 Remijan, A., Shiao, Y.-S., Friedel, D. N. et al. 2004, *ApJ*, 617, 384  
 Sandell, G., Wright, M., & Forster, J. R. 2003, *ApJ*, 590, L45  
 Shi, H., Zhao, J.-H., & Han, J. L. 2010, *ApJ*, 710, 843  
 Shu, F. H., Allen, A., Shang, H. et al. 1999, in *The Origins of Stars and Planetary Systems*, ed. C. J. Lada, & N. D. Kylafis (Kluwer Academic Press), 193  
 Scoville, N. Z., Sargent, A. I., Sanders, D. B. et al. 1986, *ApJ*, 303, 416  
 Sollins, P. K., & Ho, P. T. P. 2005, *ApJ*, 630, 987  
 Sollins, P. K., Zhang, Q., Keto, E., & Ho, P. T. P. 2005, *ApJ*, 624, L49  
 Tomisaka, K. 1998, *ApJ*, 502, L163  
 Walsh, A. J., Burton, M. G., Hyland, A. R., & Robinson, G. 1998, *MNRAS*, 301, 640  
 Wilson, T. L., & Rood, R. T. 1994, *ARA&A*, 86, 317  
 Wood, D. O. S., & Churchwell, E. 1989, *ApJS*, 69, 831  
 Wu, Y., Qin, S.-L., Guan, X. et al. 2009, *ApJ*, 697, L116  
 Zapata, L. A., Palau, A., Ho, P. T. P. 2008, *ApJ*, 479, L25  
 Zhang, Q., & Ho, P. T. P. 1997, *ApJ*, 488, 241  
 Zhang, Q., Sridharan, T. K., Hunter, T. R. et al. 2007, *A&A*, 470, 269